



Cloud occurrence, properties, and ice crystal effective dimension parameterization from nine years of far-infrared observations on the Antarctic Plateau

Elisa Fabbri¹, Tiziano Maestri¹, Michele Martinazzo¹, Federico Donat^{1, 4}, Giovanni Bianchini², Massimo Del Guasta², Gianluca Di Natale², Luca Palchetti², Guido Masiello³, Giuliano Liuzzi³, Tong Ren⁵, and Ping Yang⁵

¹Department of Physics and Astronomy "Augusto Righi", University of Bologna, Bologna, Italy

²Istituto Nazionale di Ottica, Consiglio Nazionale delle Ricerche, Italy

³Department of Engineering, University of Basilicata, Potenza, Italy

⁴Department of Physics, University of Trento, Italy

⁵Department of Atmospheric Sciences, Texas A&M University, Texas, USA

Correspondence: Tiziano Maestri (tiziano.maestri@unibo.it)

Abstract. Clouds over the Antarctic Plateau exert a strong influence on the regional radiation budget, yet observations and modelling of their properties remain scarce. Here, nine years (2012–2020) of ground-based high-resolution spectral radiance measurements from the REFIR-PAD spectroradiometer at Concordia Station (Dome C, Antarctica) are analyzed in synergy with co-located lidar observations. A machine-learning Cloud Identification and Classification (CIC) algorithm is applied to discriminate clear sky, ice cloud, and mixed-phase cloud conditions, enabling the construction of a long-term cloud climatology. Cloud optical and microphysical properties are subsequently retrieved using a simultaneous atmospheric and cloud retrieval framework, for cases with reliable cloud boundaries and cloud base heights above 500 m. Results confirm that cloud occurrence over Dome C is dominated by optically thin ice clouds, with approximately 95% of cases exhibiting optical depths below 1. Median optical depth ranges from 0.11 in summer to 0.32 in winter. The median temperature of the ice layers is approximately 237 K. Mixed-phase clouds are rare and mainly confined to the austral summer, but exhibit larger optical depths (median 1.7) and warmer temperatures (approximately 246 K). Based on the retrieved dataset, a new parameterization of ice crystal effective dimension is derived. Compared with commonly used parameterizations developed for tropical and midlatitude conditions, the proposed scheme predicts systematically smaller particle sizes, highlighting the inadequacy of existing formulations for the Antarctic environments. These results provide new observational constraints on Antarctic cloud microphysics and support improved cloud representation in climate and numerical weather prediction models.

1 Introduction

The Antarctic region plays a unique role in the global radiation budget, acting as a global energy sink. Clouds over Antarctica are a key component of the Earth's energy balance, influencing radiative fluxes both locally at high latitudes and globally through large-scale teleconnections and the modulation of atmospheric circulation patterns (Adhikari et al., 2012; Bromwich



20 et al., 2012). Several studies (e.g. Lubin et al. (1998)) have shown that variations in Antarctic cloudiness and cloud radiative properties can induce significant anomalies in global atmospheric circulation, underscoring the far-reaching climatic influence of this region. Despite their recognized importance, Antarctic clouds remain poorly characterized, mainly due to the scarcity of accurate and continuous observations (Cossich et al., 2021; Lachlan-Cope, 2010). Passive satellite observations face severe limitations: instruments operating at solar wavelengths are unavailable for approximately half of the year, while infrared sensors struggle to discriminate clouds from snow- and ice-covered surfaces (Bromwich et al., 2012). Recent comparison between cloud products derived on the Antarctic Plateau using the Infrared Atmospheric Sounding Interferometer (IASI) or local observations show important discrepancies (Donat et al., 2025). Active satellite sensors such as radar and lidar partly alleviate these issues, but they still have difficulties in detecting low-level and optically thin clouds, which dominate the Antarctic atmosphere, due to reduced sensitivity near the surface and limited vertical resolution (Chan and Comiso, 2011; Cossich et al., 2021).

30 Over the past decade, Antarctic cloud observations have advanced through a range of field and airborne campaigns across the continent and the Southern Ocean, including the PLATO field campaign at Davis Station (Guyot et al., 2022), FIRCLOUDS and subsequent studies at Dome C (Di Natale et al., 2022; Ricaud et al., 2024a; Ricaud et al., 2024b), the AWARE campaign in West Antarctica (Lubin et al., 2020), SOCRATES observations over the Southern Ocean (D'Alessandro and McFarquhar, 2023), and Antarctic traverses such as CHINARE-33 (Xu et al., 2023). Current knowledge indicates that over the Antarctic Plateau, clear sky conditions prevail for approximately 70% of the time, while ice clouds occur year-round with an annual mean frequency of about 25%. In contrast to coastal Antarctic regions, where mixed-phase clouds are relatively common, they remain exceptionally rare over the continental interior, with an annual occurrence of only 2–3%, and are observed almost exclusively during the austral summer, peaking in December and January (Ricaud et al., 2024a). At Dome C, ice cloud optical depth typically ranges between 0.1 and 5 (Di Natale et al., 2022). Despite their low frequency over the Plateau, mixed-phase clouds exert a substantial net positive radiative impact that increases with liquid water content (Ricaud et al., 2024a). Based on ground-based far-infrared observations at Dome C, Maestri et al. (2019a) retrieved ice crystal effective radii ranging from 2 to 120 μm , with a median value around 16 μm , in general agreement with previous Antarctic studies. In continental mixed-phase clouds, supercooled water droplets typically exhibit small effective diameters of around 20 μm (Bertossa et al., 2023; Ricaud et al., 2024a), with even smaller droplet radii (below 5 μm) reported at McMurdo Station (Lubin et al., 2020). Thermodynamically, ice clouds over Dome C are observed across a broad temperature range (approximately -40 to -20°C), whereas mixed-phase clouds are confined to a narrower interval between -38 and -20°C . Within this range, a near-balanced partition between ice and liquid water has been estimated at temperatures between -21 and -24°C (Xu et al., 2023).

Despite the growing observational constraints on Antarctic cloud occurrence and microphysics, their representation in climate models remains highly uncertain, largely due to the parameterization of ice cloud microphysical and radiative properties. Since climate models cannot explicitly resolve ice Particle Size Distributions (PSDs), the effective dimension is commonly adopted as a bulk variable and parameterized as a function of prognostic model variables, such as temperature and ice water content (Boudala et al., 2002; McFarquhar et al., 2003; Sun and Rikus, 1999). As a result, cloud radiative properties in both Global Circulation Models (GCMs) and Numerical Weather Prediction (NWP) systems strongly depend on the chosen microphysical parameterization. For instance, Bozzo et al. (2008) showed that representing mid-latitude cirrus clouds with a



55 realistic mixture of crystal shapes, rather than simplified spheres, introduces systematic biases in 2m temperature and short-
wave (SW) and long-wave (LW) fluxes from the very start of the simulation. In addition, Weverberg et al. (2013) demonstrate
that the simulation of Mesoscale Convective Systems (MCS) is extremely sensitive to microphysical parameterizations, with
the sedimentation speed of ice condensate, which in turn depends on particle effective dimensions, identified as the key factor
controlling cloud morphology. Finally, Muskatel et al. (2021) show that variations in effective particle size (5–200 μm) can
60 change surface radiation by approximately 10% in NWP simulations.

Several parameterizations of the ice cloud effective dimension have been proposed, mostly based on in situ observations
from midlatitude, tropical, or Arctic environments. Ou and Liou (1995) introduced one of the earliest schemes, in which the
effective dimension is expressed solely as a polynomial function of temperature. Wyser (1998) extended this approach by
parameterizing the effective radius as a function of both temperature and ice water content (IWC), assuming hexagonal col-
65 umn ice crystals and introducing a gamma particle size distribution to better represent small particles. Sun and Rikus (1999)
proposed a simplified formulation derived from McFarquhar and Heymsfield (1997), specifically designed for ease of imple-
mentation in NWP and GCM frameworks, again relying on temperature and IWC as predictors. More complex schemes have
also been developed. McFarquhar et al. (2003) introduced a parameterization of the effective radius based on observations of
tropical anvil clouds associated with deep convection, incorporating detailed information on ice crystal shape and explicitly
70 accounting for intrinsic uncertainty by providing ranges of fitting coefficients rather than single deterministic values. Bozzo
et al. (2008) defined an optical property parameterization of midlatitude cirri by prescribing temperature and ice content de-
pendent mixtures of ice crystal habits, with the relative contribution of each habit determined through weighting over observed
particle size distributions. Heymsfield et al. (2014) proposed relationships based on a large set of in situ data spanning from the
Arctic to the tropics, with cloud temperatures ranging from 0 to -86°C . Finally, the scheme proposed by Boudala et al. (2002)
75 is particularly relevant for polar applications, as it was developed specifically for stratiform ice clouds using data acquired at
latitudes above 45°N . Despite their widespread use, most existing parameterizations have been derived from datasets collected
in midlatitude, tropical, or, in some cases, Arctic environments. Their applicability to Antarctic conditions therefore remains
uncertain (Lachlan-Cope, 2010).

In this study, we analyze a large dataset of high-resolution spectral measurements of downwelling radiance acquired between
80 2012 and 2020 by the REFIR-PAD (Radiation Explorer in the Far Infrared – Prototype for Applications and Development)
instrument at the Concordia Research Station (Dome C) on the Antarctic Plateau (Palchetti et al., 2015). The use of a ground-
based passive spectral sensor offers the key advantage of exploiting the strong radiative contrast between clouds and the
cold background space (Donat et al., 2025; Cossich et al., 2021). Moreover, measurements in the far-infrared spectral region
(below 667 cm^{-1}) have been shown to enhance traditional mid-infrared techniques by improving cloud detection, classification,
85 and the retrieval of cloud microphysical properties (Di Natale et al., 2020a; Maestri et al., 2019a). The unique REFIR-PAD
dataset is exploited to retrieve cloud geometrical, optical, and microphysical properties over the Antarctic Plateau. Based on
these long-term ground-based far-infrared observations, we derive a new parameterization of the effective dimension of ice
crystals specifically tailored to Antarctic ice clouds. Unlike most existing schemes, which rely on in situ measurements, the
proposed scheme is derived entirely from remote-sensing measurements, providing an observationally based alternative to



90 existing schemes predominantly constrained by non-Antarctic in situ data. To our knowledge, this study provides one of the longest ground-based far-infrared observational records of Antarctic clouds and represents the first attempt to derive an ice cloud microphysical parameterization based exclusively on such measurements.

2 Data and methods

2.1 Dataset

95 Measurements of downwelling high-resolution spectral radiance are acquired using the REFIR-PAD (Radiation Explorer in the Far Infrared – Prototype for Applications and Development) instrument, which is installed in an insulated Physics Shelter approximately 500 m south of the Italian–French Concordia Research Station at Dome C (75°06'S, 123°23'E), on the Antarctic Plateau at an elevation of 3,233 m above sea level. REFIR-PAD is a ground-based Fourier Transform Spectroradiometer (FTS) designed to perform high-resolution spectral measurements of downwelling radiance in the far-infrared and part of the mid-infrared region, covering a spectral range of 100 – 1500 cm⁻¹ with a resolution set to 0.4 cm⁻¹ (Bianchini et al., 2019).
100 This range accounts for a substantial portion of the atmospheric long-wave emission. The dataset used in this study spans a nine-year period, from January 2012 to December 2020. Under normal operating conditions, the instrument provides spectral radiance measurements approximately every 14 min. To achieve this, the instrument points at the zenith through a 1.5 m chimney. For each scene measurement, the instrument performs a sequence of four calibration acquisitions using internal reference
105 blackbody sources, followed by four sky observations. Each acquisition takes about 80 s, and considering additional delays for detector settling after scene changes, the entire sequence lasts about 14 min. Furthermore, the instrument alternates between cycles of 5 to 6 hours of measurement and 1 to 3 hours of data preprocessing.

Along with interferometric measurements, backscattering and depolarization profiles acquired by a tropospheric backscattering lidar (Light Detection and Ranging) (INO-CNR Istituto Nazionale di Ottica) are used. Their use serves as a twofold
110 purpose: i) determine the scene truth for selecting the training and test sets required for the classification task, and ii) determine the cloud geometrical features (mainly the bottom and top heights), which serve as a priori information during the retrieval process. The lidar instrument, installed in the same Physics Shelter as REFIR-PAD, is an active remote sensing device that emits polarized beams of radiation in the visible band, at 532 nm, and detects backscattering and depolarization signals up to 7 km above the ground, providing measurements every 10 min.

115 2.2 Algorithms

2.2.1 Cloud classification and identification (CIC) algorithm

The Cloud Identification and Classification (CIC) algorithm is used for scene classification. The algorithm is designed to classify three different conditions: clear sky, ice clouds, and mixed-phase clouds. The latter are observed exclusively during the warm macro-season, which spans from November to March. The CIC algorithm was originally developed by Maestri et al.
120 (2019b), and is adopted as scene classifier in the End-to-End Simulator (FE2ES) (Sgheri et al., 2022) of the Far-infrared



Outgoing Radiation Understanding and Monitoring (FORUM) mission (Palchetti et al., 2020), currently under development by ESA as its ninth Earth Explorer mission. Performance evaluation studies of the algorithm have been conducted under various conditions and observational geometries (Maestri et al., 2019a; Cossich et al., 2021; Magurno et al., 2020). The algorithm is particularly advantageous compared to other methods when the training set contains a small number of samples. In this study, the updated version proposed by Donat et al. (2024) is used, as it offers increased sensitivity to thin clouds and improved classification performances.

The application of the CIC to the REFIR-PAD observations is required to allow the derivation of the scene conditions before the application of the retrieval of the atmospheric and cloud properties. In the present work, the updated CIC is applied to an extended dataset with respect to what shown in Cossich et al. (2021) and trained using spectra from the entire timeframe analyzed so that the time series can be analyzed avoiding possible biases.

A detailed description of the algorithm, is found in Maestri et al. (2019b) (the original algorithm) and Donat et al. (2024) (the updated version), but the key steps are summarized below for reader convenience:

1. A training set (TS_X) is defined for each class X under consideration: clear sky and ice clouds from April to October, and clear sky, ice clouds, or mixed-phase clouds from November to March.
2. For each training set TS_X , the eigenvectors (ϵ_{TS_X}) and eigenvalues (λ_{TS_X}) of the covariance matrix are computed and sorted in descending order of eigenvalues. To reduce spectral noise, only a limited number of principal components are retained, following the criteria described in Turner et al. (2006) and Malinowski (2002).
3. When a new input spectrum \mathbf{x} is classified, an extended training set (ETS_X) is created for each class by adding \mathbf{x} to the corresponding original training set (TS_X).
4. For each extended training set ETS_X , the principal components are calculated as described in point 2.
5. For each class X , the similarity between the original and extended training sets is quantitatively evaluated using two indices: $SI_{eigVec}(\mathbf{x}, X)$, based on eigenvectors, and $SI_{eigVal}(\mathbf{x}, X)$, based on eigenvalues. Their formal definitions can be found in Donat et al. (2024) (Eqs. (8) and (9)).
6. Finally, for each pair of classes (X_1 and X_2), two similarity index differences (SIDs) are computed as $SID(\mathbf{x}, (X_1, X_2)) = SI(\mathbf{x}, X_1) - SI(\mathbf{x}, X_2)$, yielding SID_{eigVec} and SID_{eigVal} . These two indices are used to determine the most likely class for the input spectrum \mathbf{x} , through a linear decision boundary applied to the SID space.

With respect to the spectral band covered by the REFIR-PAD instrument, the algorithm performs classification using only a restricted spectral range of $380\text{--}1000\text{ cm}^{-1}$. This range was determined through an optimization procedure (hyperparameter tuning) described in Cossich et al. (2021), as it was found to provide the best classification performance for Antarctic sky conditions. Overall, the CIC algorithm demonstrates a high capability to discriminate cloud phase and presence under Antarctic conditions, including optically thin clouds that are typically challenging for satellite-based approaches. This robustness is a key prerequisite for deriving reliable long-term cloud statistics from ground-based spectral observations.



2.2.2 Training/test set selection and evaluation metrics

The algorithm is trained and tested on a subset of the REFIR-PAD acquired radiances, consisting of 70 spectra for each class in the training sets and 130 elements for each class in the test set. The spectra are selected by visually inspecting the co-located lidar backscattering and depolarization profiles. The criteria adopted for the selection of the spectra consist in the individuation of neatly defined cases observed by the lidar. To represent the natural variability, we aimed at choosing scenes with clouds at different heights (and temperatures), homogeneously distributed throughout the nine-years considered period. The performance of the algorithm is evaluated on the test set using three standard metrics for each class i : Hit Rate (HR), Threat Score (ThS), and Positive Predictive Value (PPV). Their definitions are summarized in Table 1. To better analyze misclassifications, we also compute the misclassification ratio $m_{i \rightarrow j}$, defined in Eq. (1).

Table 1. Definition of performance metrics for class i . TP, FP and FN indicate True Positives, False Positives and False Negatives respectively.

Metric	Definition
HR_i	$\frac{TP_i}{TP_i + FN_i}$
ThS_i	$\frac{TP_i}{TP_i + FN_i + FP_i}$
PPV_i	$\frac{TP_i}{TP_i + FP_i}$

Here, TP_i is the number of correctly classified elements of class i , FN_i are elements of class i misclassified as another class, and FP_i are elements of other classes incorrectly assigned to class i . The misclassification ratio $m_{i \rightarrow j}$ represents the probability that a class- i element is misclassified as class j :

$$m_{i \rightarrow j} = \frac{FN_{i \rightarrow j}}{TP_i + FN_i} \quad (1)$$

where $FN_{i \rightarrow j}$ is the number of class- i elements classified as class j .

2.2.3 Uncertainty assessment of the classification results

Classification results over the entire dataset are used to derive annual and seasonal cloud-occurrence statistics and to investigate their relationship with surface temperature. Following Cossich et al. (2021), the uncertainties in the percentage occurrences are estimated from the HR values computed on the test set. Since the performance of the CIC algorithm over the complete dataset is unknown, the underlying assumption is that the HR values evaluated on the test set are representative of the whole dataset. From the definition of HR_i in Table 1, the number of misclassified spectra for class i can be computed. HR_i represents the probability that a spectrum belonging to class i is correctly classified by the CIC algorithm, formally $HR_i = N_i^{CIC} / N_i^{true}$, where N_i^{CIC} is the number of spectra classified as belonging to class i by the CIC algorithm and N_i^{true} is the total number of spectra truly belonging to class i . The complementary probability, representing the likelihood that the CIC algorithm misclassifies a



spectrum from class i , is given by $1 - \text{HR}_i$. Therefore, the number of misclassified spectra can be calculated as:

$$N_i^{\text{err}} = N_i^{\text{true}} \cdot (1 - \text{HR}_i) \quad (2)$$

Since N_i^{true} is unknown for the complete dataset, it can be estimated from the HR_i definition as $N_i^{\text{true}} = N_i^{\text{CIC}} / \text{HR}_i$. By substituting into the equation above and dividing by N_i^{TOT} (the total number of spectra of class i in the test set) one obtains the percentage error:

$$\epsilon_{\%} = \frac{N_i^{\text{CIC}}}{N_i^{\text{TOT}}} \cdot \frac{1 - \text{HR}_i}{\text{HR}_i} \cdot 100 \quad (3)$$

Because the test set does not necessarily encompass the full diversity and complexity of real-world cases encountered in operational conditions, the reported error should be interpreted as an approximate lower bound on the true classification error.

2.2.4 Retrieval lidar (RetLid) and simultaneous atmospheric and cloud retrieval (SACR) algorithms

When the CIC identifies a spectrum as cloudy, the cloud geometrical, radiative, and microphysical properties are retrieved using the Simultaneous Atmospheric and Cloud Retrieval (SACR) algorithm. Specifically, the cloud bottom height (CBH) and the cloud top height (CTH) are inferred using the RetLid algorithm, based on the work of Van Tricht et al. (2014), applied to co-located lidar measurements. The algorithm simultaneously processes backscattering and depolarization signals to retrieve the final CTH and CBH. To estimate CTH and CBH, initial signal and minimum altitude thresholds are applied to both backscattering and depolarization values, derived from extensive sensitivity tests. Specifically, the depolarization signal is utilized starting from 20m above ground level (AGL), whereas the backscattering signal is analyzed from 200m upwards, due to the intense molecular backscattering in the lower layers which would otherwise be indistinguishable from a potential cloud signal. The algorithm performs signal smoothing and calculates the vertical derivative for both signals. Negative values indicate a decrease in signal intensity, while positive values represent an increase; consequently, the relative minima and maxima correspond to the top and bottom positions, respectively. To retrieve accurate CTH and CBH values from the backscattering signal, the algorithm starts with initial values of -1 and spatial derivative thresholds set at $\pm 3 \times 10^{-6}$ in arbitrary unit (AU). It then iteratively adjusts these thresholds to converge on CTH and CBH values such that $\text{CTH} > \text{CBH}$, corresponding to the extremes of the negative and positive derivatives. Regarding the depolarization signal, the thresholds remain fixed, and the minima and maxima of the derivatives are calculated directly. The final heights are determined by comparing the outputs obtained from both signals.

Successively, the CIC-identified cloudy REFIR-PAD spectra are analyzed by the SACR algorithm for the retrieval of cloud parameters. Derived properties include optical depth, effective dimension of ice crystals and water droplets (corresponding to effective diameter in this case), atmospheric profiles of water vapor and temperature, the ice fraction, γ , defined as the ratio of the ice water path (IWP) to the sum of IWP and liquid water path (LWP), and the instrumental parameters such as the frequency stretch and the mixing coefficient (Di Natale et al., 2020b) of the instrument line shape (ILS). The SACR code, developed by Di Natale et al. (2020b), comprises a forward model capable of simulating spectral radiance in the presence of ice/liquid and mixed-phase clouds, over the entire long-wave interval (from 100 to 3000 cm^{-1}); however, only the spectral



interval between 200 and 980 cm^{-1} is used for the retrieval, as it is less affected by measurement noise. The model uses the a priori information of the CBH and CTH derived from the RetLid algorithm which are fixed parameters in the radiative transfer simulation; the cloud optical coefficients are instead sourced from specific databases developed by Ping Yang and colleagues (Yang et al., 2013) averaged over typical Γ -particle size distributions and tabulated as a function of the effective diameters as defined in Yang et al. (2005). SACR includes a retrieval algorithm based on the optimal estimation (OE) approach and the Levenberg-Marquardt (LM) (Levenberg, 1944) iterative formula, where the solution is found by minimizing iteratively the cost function defined in Eq. (4):

$$\chi^2 = (\mathbf{y} - \mathbf{F}(\mathbf{x}))^T \mathbf{S}_y^{-1} (\mathbf{y} - \mathbf{F}(\mathbf{x})) + (\mathbf{x} - \mathbf{x}_a)^T \mathbf{S}_a^{-1} (\mathbf{x} - \mathbf{x}_a) \quad (4)$$

Here, \mathbf{y} represents the vector of radiance measurements, \mathbf{x} denotes the state vector containing the atmospheric parameters to be retrieved, \mathbf{F} is the forward-simulated spectrum, and \mathbf{x}_a is the vector of a priori parameters. The matrices \mathbf{S}_y and \mathbf{S}_a denote the error Variance-Covariance Matrices (VCM) of the measurements \mathbf{y} and the a priori estimate \mathbf{x}_a , respectively.

For CIC-identified ice clouds, a homogeneous population of solid single-column ice crystals is assumed. For mixed-phase clouds, the retrieval estimates the relative contributions of liquid water droplets and ice crystals by fitting γ .

The retrieval is restricted to cases classified as cloudy by the CIC algorithm, with available collocated lidar observations and CBH above 500m AGL. This selection accounts for the increased uncertainty in cloud boundary detection at lower altitudes, primarily due to the frequent occurrence of precipitating clouds (including virga) and diamond dust. The 500m threshold is therefore adopted as a conservative choice to favour more robust cloud boundary information and to limit uncertainties in the retrieved optical and microphysical properties.

Retrievals are further filtered based on quality criteria. Cases with a retrieval χ^2 greater than 2 are discarded, as they indicate a lack of convergence in the inversion procedure. In addition, retrievals with an optical depth lower than 0.02 or greater than 5 are excluded. These thresholds prevent the inclusion of extremely thin layers (e.g., associated with diamond dust or fragmented clouds) and avoid saturation effects in the interferometric observations.

It is important to note that the retrieval relies on several simplifying assumptions, including the assumption of vertically homogeneous cloud properties and prescribed ice particle habits. In addition, uncertainties in the lidar-derived cloud boundaries may propagate into the retrieval of optical and microphysical properties. While the applied filtering criteria (e.g., CBH larger than 500m, and the χ^2 threshold) are designed to minimize these effects, residual uncertainties may still influence the retrieved parameters and should be considered when interpreting the results.

3 Cloud classification

A dataset of radiances acquired by REFIR-PAD, comprising 232,999 spectra, is analyzed using the CIC algorithm. We computed the metrics discussed in Section 2.2.2, as obtained by the CIC algorithm for each specific class in the test set and for the two different macro-seasons: the cold and the warm one. The results, in percentage for HR, ThS, and PPV, are summarized in Fig. 1, and the $m_{i \rightarrow j}$ values (also expressed as percentages) are shown in Fig. 2. The algorithm achieved excellent



240 performance in all classes, with HR scores consistently higher than 95%. During the warm season, the predominant source
of classification error arises from the misclassification of mixed-phase clouds as ice clouds. This occurs in approximately
4.6% of scenes affected by mixed-phase clouds, as shown in Fig. 2. Importantly, this type of error concerns the classification
of cloud phase rather than cloud identification. The other metrics are also able to catch the difficulties in distinguishing the
cloud phase: mixed-phase clouds exhibit the lowest HR, while the ice cloud class shows the lowest ThS and PPV. The results
245 indicate, respectively, a lower probability of correctly classifying mixed-phase clouds and a higher number of false positives
for cases classified as ice clouds. The opposite error, i.e. classifying ice clouds as mixed-phase clouds, is less frequent, with a
misclassification ratio below 1%. Notably, in the warm season, the mixed-phase and clear sky classes are never confused by
the classifier. However, some misclassifications occur between the ice cloud and clear sky classes, with more cases of clear sky
being misclassified as ice clouds than vice versa.

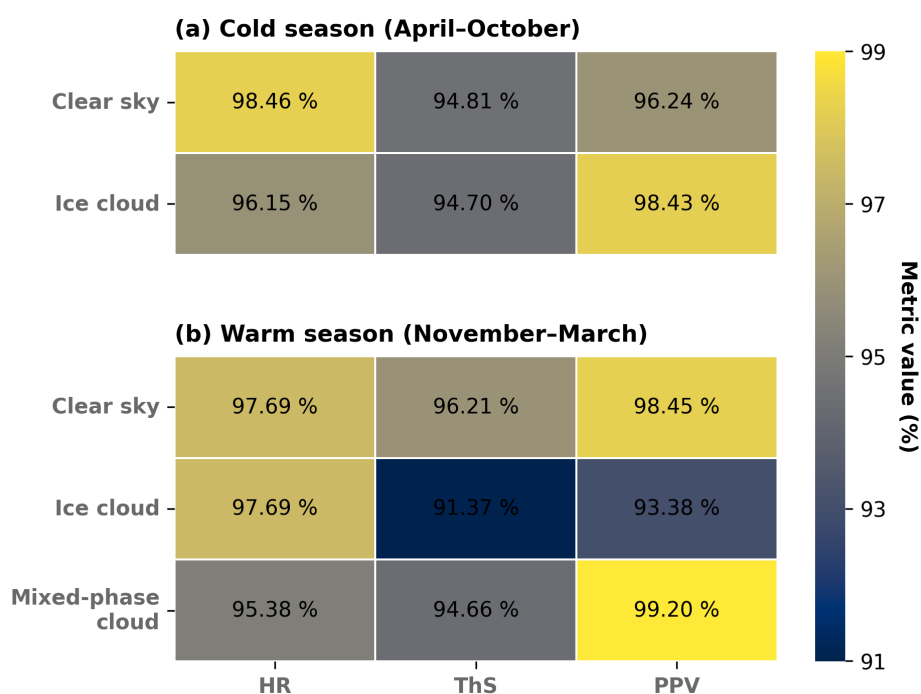


Figure 1. HR, ThS and PPV (in percentage) of the CIC algorithm for different classes. The warm and the cold season are analyzed separately. A value of 100% indicates perfect performance.



250 During the cold season, the opposite situation is observed, with ice clouds more frequently misclassified as clear sky (3.85 % of cases) than the other way (1.54%). This is also reflected in the other metrics: ice clouds exhibit a lower HR and a higher PPV, whereas clear skies show the opposite pattern. The classification results show that clear sky conditions account for $67.7 \pm 1.3\%$

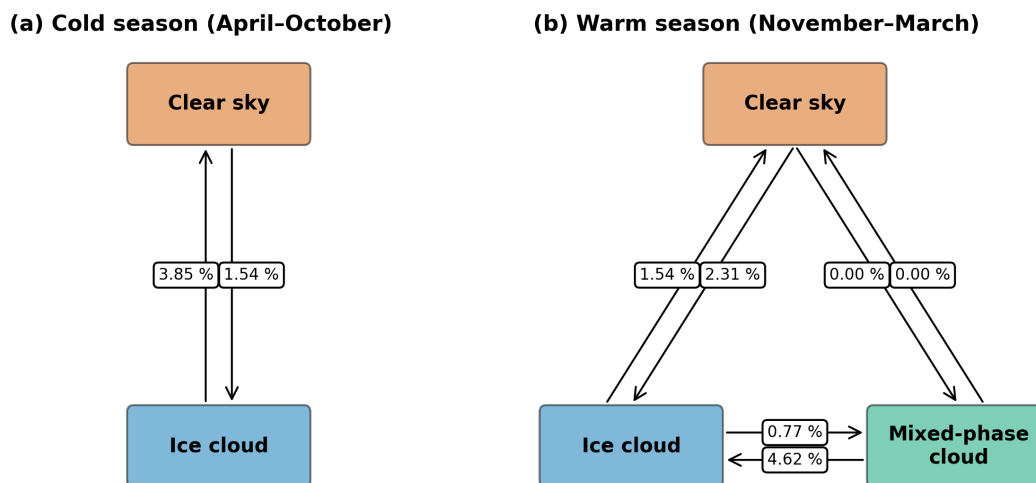


Figure 2. Misclassification percentage values, $m_{i \rightarrow j}$, for each class pair across the two macro-seasons.

of the total, ice clouds for $29.6 \pm 0.9\%$, and mixed-phase clouds for $2.63 \pm 0.13\%$; unclassified spectra represent 0.02% of the total.

255 Annual means (in percent) for each class are also computed, and the results are presented in Fig. 3, with shaded areas representing the associated uncertainties. The percentages of unclassified spectra are shown in the gray box at the bottom of the figure, whereas the percentage temporal coverage of the total analyzed observations, assuming a 14 minutes acquisition interval, is displayed at the top of the figure for the warm and cold periods of each year. The total cloud occurrence, which is the sum of ice clouds and mixed-phase clouds, shows significant inter-annual variability. The highest value is recorded in

260 2012 ($40.6 \pm 1.5\%$), while the lowest occurs in 2013 ($25.5 \pm 1.0\%$). Notably, these two years also represent the extremes for mixed-phase cloud occurrence: 2012 has the highest value ($6.4 \pm 0.3\%$), while 2013 has the lowest ($1.52 \pm 0.07\%$). The two years mentioned above also have the lowest annual temporal coverage in the dataset, with values around 30%. This limited coverage contrasts with other years, which show an increasing trend in temporal coverage, ranging from 65% in 2015 to a maximum of 91% in both 2019 and 2020. In 2012, the temporal coverage during the warm season, when mixed-phase clouds

265 are typically present, was substantially higher than during the cold season. In contrast, 2013 exhibits the opposite pattern, with REFIR-PAD observations more densely distributed in the cold season than in the warm season. This imbalance in seasonal sampling likely leads to an overestimation of mixed-phase cloud occurrence and total cloudiness in 2012, and a corresponding underestimation in 2013. Note that the annual mean statistics are consistent, within the correspondent uncertainties, with those

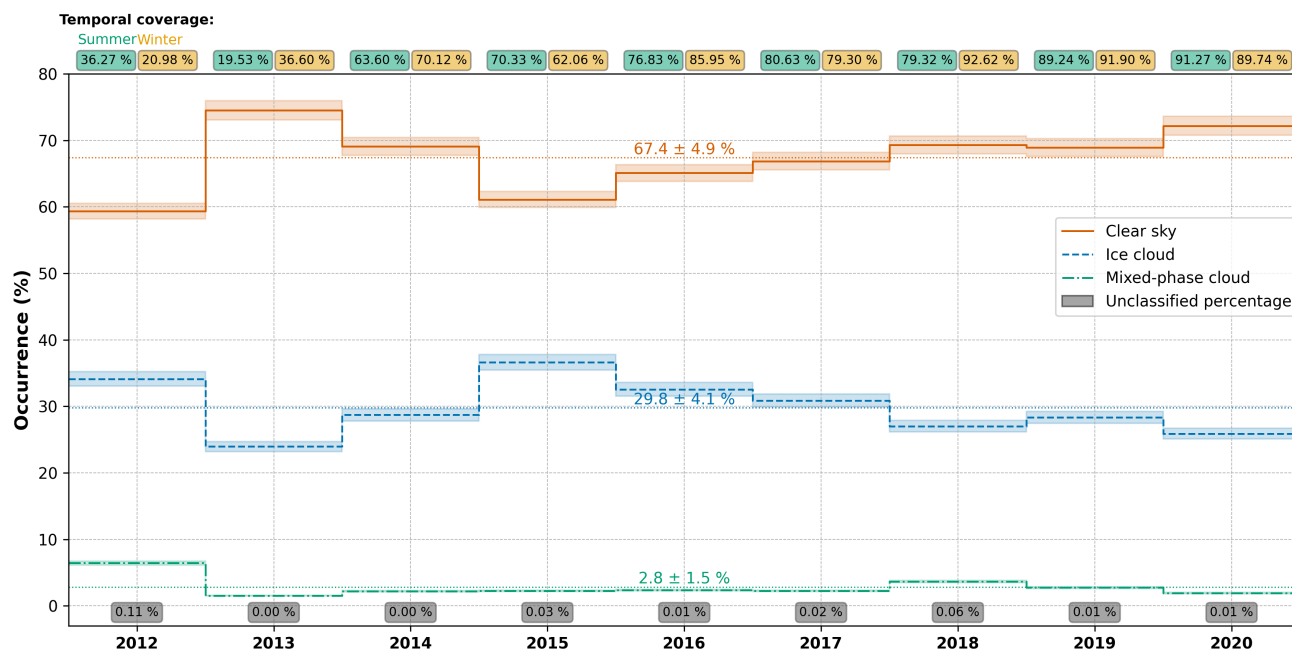


Figure 3. Annual mean occurrences of clear, ice cloud and mixed-phase cloud classes. The mean value is also plotted. Uncertainties are represented by shaded areas. The box at the bottom of each year reports the percentages of unclassified spectra. Temporal coverages of the analyzed measurements (in percent) for the warm and the cold season are also indicated at the top of the figure for each year.

presented by Cossich et al. (2021), which evaluated cloud occurrence for the 2012–2015 period using a training set based exclusively on spectra selected from 2012.

The average seasonal cloud occurrence is also evaluated, and the results are presented in Fig. 4, where the shaded areas represent one standard deviation from the mean occurrence. The mean cloud occurrence ranges from a minimum of $26 \pm 4\%$ in the austral fall (MAM) to a maximum of $45 \pm 5\%$ in austral summer (DJF). Although mixed-phase clouds are present almost only in summer, their occurrence peaks at $10 \pm 4\%$ during this period, accounting for approximately 22.80% of the total cloud cover for the season. The present results extend and update what was reported in Cossich et al. (2021) which was affected by the limited temporal coverage of the dataset and by the nonuniform sampling of the measurements throughout the years and seasons. The monthly time series of the percentage occurrence of ice clouds (left panel), together with the corresponding Fourier transform (right panel), is shown in Fig. 5 to identify the dominant periodicities in the seasonal and interannual variability of the occurrence of ice clouds. To avoid potential biases related to the limited and unevenly distributed observations throughout the year, data from 2012 and 2013 are excluded from the analysis. The significance of the spectral peaks is assessed at the 95% confidence level using 10,000 red-noise simulations, following the methodology described in Donat et al. (2025) and applied to cloud occurrence, surface temperature, and pressure. The analysis reveals a significant semi-annual cycle in Antarctic ice cloud occurrence, with maxima in January and July, consistent with previous observations by

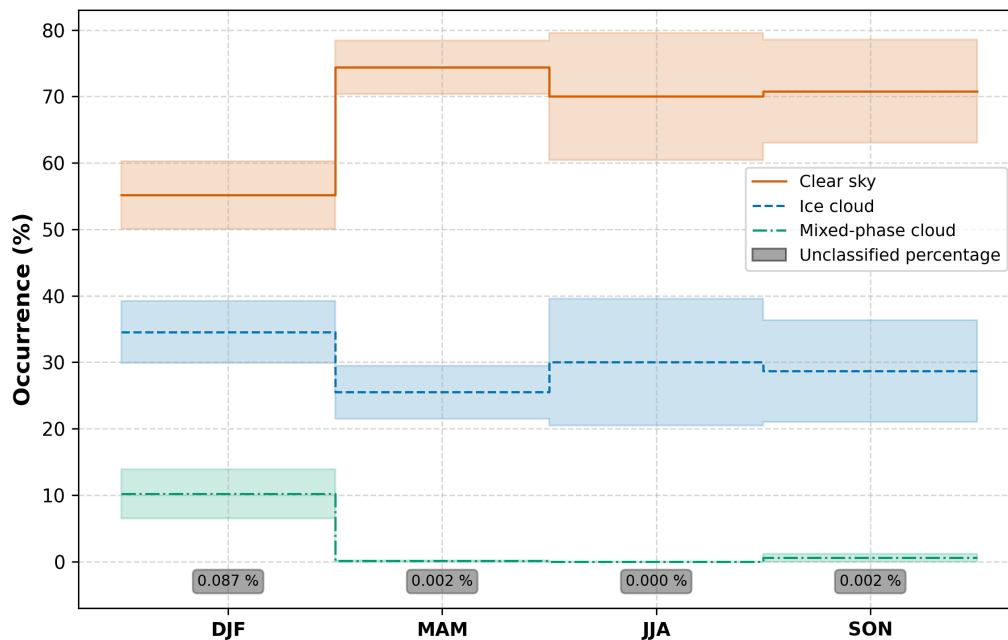


Figure 4. Seasonal cloud and clear sky occurrence in the period 2012-2020. Shaded areas represent one standard deviation from the mean.

Donat et al. (2025), which considered all cloud types (ice and mixed-phase). In the present analysis, no significant annual cycle is detected, suggesting that mixed-phase clouds are essential in generating an annual cycle in the total Antarctic cloud occurrence.

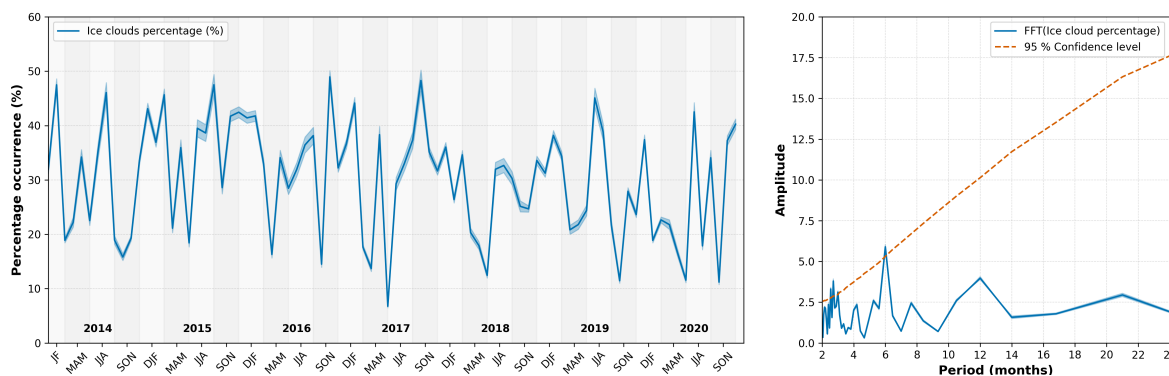


Figure 5. Monthly percentage occurrence of ice clouds. The left panel shows the 2014–2020 time series, with shaded areas representing the uncertainty associated with the classification, while the right panel shows the corresponding Fourier transform analysis.

Data from the Osservatorio Meteo-Climatologico Antartico are used to investigate the relationship between cloud (presence and phase) and surface temperature. Each sky classification obtained from the REFIR-PAD observations is matched with the



hourly surface temperature measurement to investigate possible correlations between cloudiness and temperature at the ground.

290 The results are shown in Fig. 6, where each class (clear sky, ice cloud, and mixed-phase cloud) is plotted as a function of surface temperature. The total number of observations in each temperature bin is indicated at the base of the corresponding bar. Table 2 reports the median and median absolute deviation (MAD) of surface temperature for all-sky conditions and seasons. The median and MAD, defined as the median of the absolute deviations from the data median, are used instead of the mean and standard deviation due to their greater robustness against outliers and asymmetric distributions. Although temperature ranges

295 vary considerably with the season (from 213K to 257K in austral summer, and from approximately 195K to 245K in the other seasons), both ice clouds and mixed-phase clouds are consistently associated with warmer near-surface air conditions. The cloud radiative effect cannot be directly measured from the available observations. However, an indication can be inferred from the difference between near-surface air temperature under all-sky conditions and under clear sky conditions (last and second columns of Table 2, respectively). For all seasons, the near-surface air temperature is, on average, more than 2 K higher

300 in all-sky conditions than is clear sky conditions, reaching approximately 3 K during austral spring (SON) and winter (JJA). Notably, during JJA, incoming solar radiation is negligible, so cloud radiative forcing is provided by long-wave emission and scattering only.

Table 2. Median surface temperature \pm MAD under different sky conditions.

	Clear sky	Ice cloud	Mixed-phase cloud	All cloud	All-sky
DJF	238.1 \pm 5.7 K	239.5 \pm 5.1 K	244.2 \pm 2.6 K	241.1 \pm 4.6 K	239.5 \pm 5.2 K
MAM	210.1 \pm 4.5 K	218.5 \pm 5.2 K	227.7 \pm 2.0 K	218.5 \pm 5.3 K	212.1 \pm 5.3 K
JJA	205.8 \pm 4.1 K	216.7 \pm 5.6 K	-	216.7 \pm 5.6 K	208.3 \pm 5.5 K
SON	217.1 \pm 7.4 K	225.1 \pm 7.4 K	239.0 \pm 3.0 K	225.3 \pm 7.5 K	220.1 \pm 8.6 K
All season	213.0 \pm 8.4 K	224.0 \pm 9.3 K	244.0 \pm 2.7 K	225.3 \pm 10.3 K	217.0 \pm 10.4 K

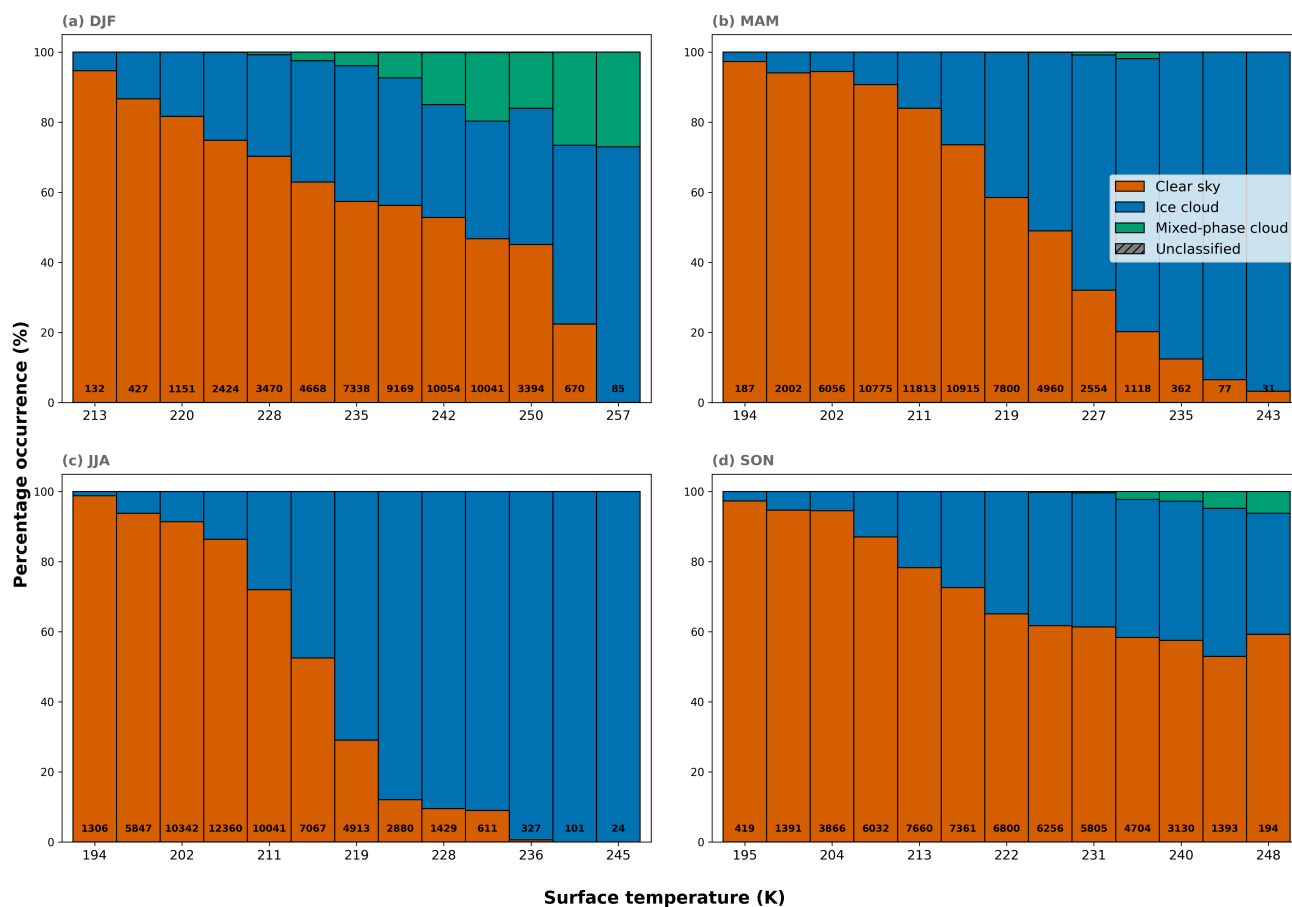


Figure 6. Seasonal occurrence of each class (clear sky, mixed-phase cloud, ice cloud) as a function of surface temperature. The total number of observations for each temperature bin is reported at the bottom of each bin. Each panels refers to a season: a) summer, b) fall, c) winter, d) spring.



4 Analysis of the retrieved cloud properties

Figure 7 illustrates the selection process, starting from all clouds identified by the CIC algorithm and ending with the subset used for property retrieval, with the percentages of clouds shown for each step. From the entire dataset spanning 2012-2020, a total of 75,137 spectra are classified as cloudy by the CIC algorithm (either ice or mixed-phase). Among these, only 14,901 spectra (14,396 ice clouds and 505 mixed-phase clouds) are used for the retrieval of cloud properties, corresponding to those cases characterized by CBH above the 500m AGL. The threshold on CBH is obtained using the lidar observations. For more information about the seasonal and inter-annual relative frequency of ice and mixed-phase clouds we refer the reader to Appendix A.

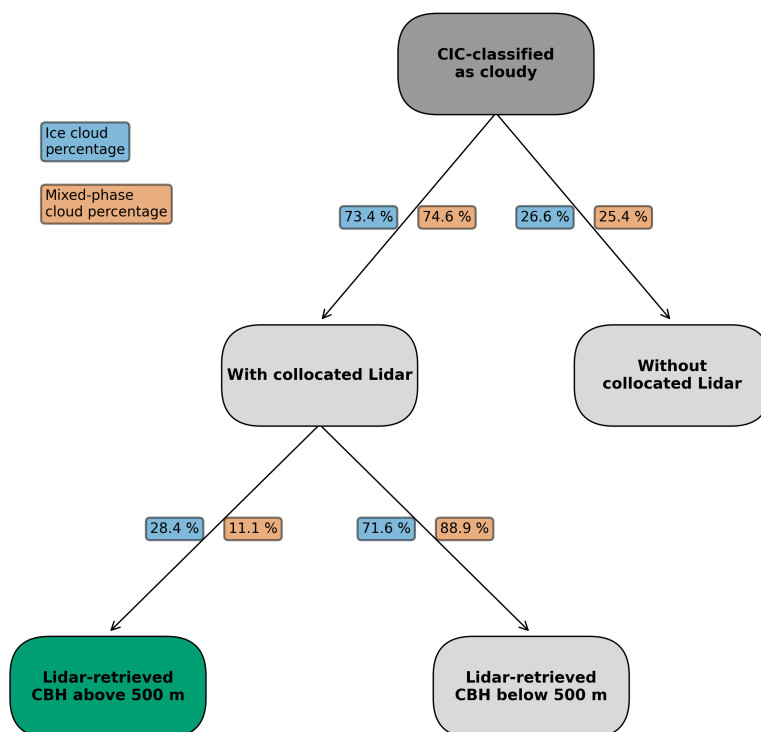


Figure 7. Flow diagram showing the selection of clouds for property retrieval.

Among the data considered for the retrieval, convergence is achieved in 94% of cases for both ice and mixed-phase clouds. Clouds with retrieved optical depths, τ , outside the range $0.02 \leq \tau \leq 5$ are excluded from the analysis. In case of ice clouds, only 0.1% of the data falls below 0.02 optical depths, and no cases exceed 5. For mixed-phase clouds, we do not find cases with optical depth below 0.02, while 10.1% of the remaining data exceed the upper limit of 5. The annual distribution of the



315 remaining spectra, separated into CIC-classified ice clouds, mixed-phase clouds, and total cloudy observations, is reported in Table 3, while Table 4 shows the monthly number of analyzed ice clouds.

Table 3. Number of observations used in the analysis for each year from 2012 to 2020.

Year	2012	2013	2014	2015	2016	2017	2018	2019	2020	Total
N_{Ice}	0	46	1,315	1,462	2,490	2,086	1,927	1,991	2,194	13,511
N_{Mixed}	12	11	47	3	52	110	123	46	22	426
N_{total}	12	57	1,362	1,465	2,542	2,196	2,050	2,037	2,216	13,937

Table 4. Number of ice observations used in the analysis for each month.

Month	Jan	Feb	Mar	Apr	May	Jun	Jul	Aug	Sep	Oct	Nov	Dec	Total
N_{Ice}	1,761	1,357	1,565	814	912	611	1,449	1,118	1,183	627	972	1,142	13,511

4.1 Ice clouds

Figure 8 shows histograms of retrieved ice cloud properties from the SACR and RetLid algorithms. The analyzed properties include optical thickness τ (upper left panel), CBH (upper right panel), mean cloud temperature $\langle T_{\text{cloud}} \rangle$ (lower left panel), and mean effective ice crystal dimension $\langle D_{\text{eff, ice}} \rangle$ (lower right panel). The distributions are characterized using the median and the MAD, which are annotated in the plots. The distribution of τ values is fitted using a generalized lognormal distribution (Eq. (5)) over the $0.02 \leq \tau \leq 5$ range:

$$f(x'; \mu, \sigma) = \frac{1}{\sigma x' \sqrt{2\pi}} \exp\left(-\frac{(\ln x' - \mu)^2}{2\sigma^2}\right), \quad \text{where } x' = x - t, \quad (5)$$

where μ and σ are the lognormal parameters and t is a shift parameter. Unlike the standard lognormal formulation, the inclusion of t offsets the independent variable, allowing accurate fits even when the distribution does not start at zero. The fitted parameters (μ , σ , and t) and corresponding R^2 values are shown in the plot.

Antarctic ice clouds are generally optically thin, with optical depth clustered around small values, as indicated by the low median and MAD values. Approximately 95% of ice cloud cases are characterized by optical depths less than 1. The distribution exhibits a long right tail toward higher τ values and is well fitted by generalized lognormal distribution, yielding coefficients of determination R^2 greater than 0.95. Regarding temperatures, the central 90% of the distribution spans approximately 226–247 K. The effective dimension of ice particles is small, with a median of 23 μm . For comparison, Järvinen and

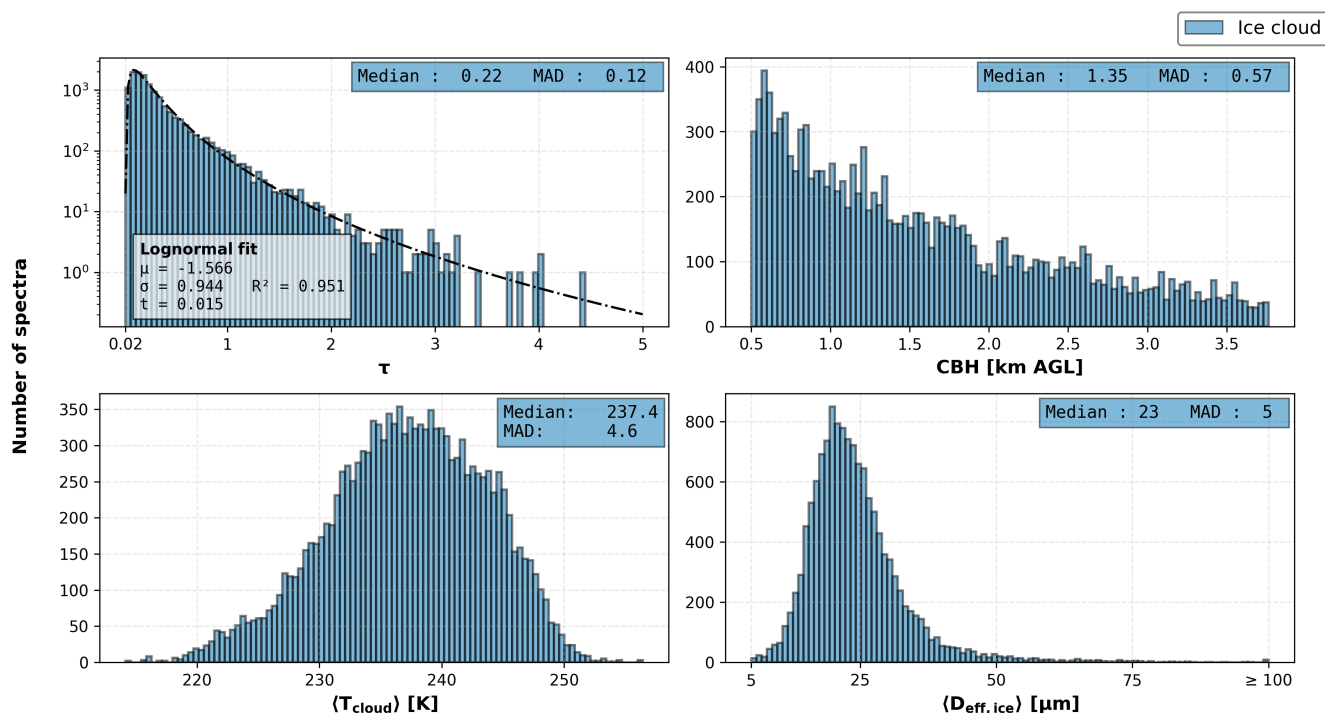


Figure 8. Histograms of ice cloud properties. The upper-left panel shows the distribution of cloud optical depth τ , with the black dashed line representing a generalized lognormal fit with parameters value and R^2 reported in the legend. The upper-right panel shows the CBH distribution. The lower-left panel plots the distribution of the mean cloud temperature $\langle T_{\text{cloud}} \rangle$, while the lower-right panel shows the distribution of the effective ice crystal dimension $\langle D_{\text{eff, ice}} \rangle$.

Schnaiter (2026) found median effective dimensions of approximately $72\mu\text{m}$ and $75\mu\text{m}$ from in-situ measurements of mid-latitude and Arctic cirri respectively. While this difference reflects the genuinely distinct microphysical environment of the Antarctic Plateau, part of the discrepancy may also arise from differences in retrieval methodology and instrumentation. The predominance of optically thin ice clouds is consistent with the low moisture content and stable atmospheric conditions typical of the Antarctic Plateau. These clouds, although radiatively subtle on an individual basis, can exert a significant cumulative impact on the surface energy balance due to their high frequency of occurrence.

Since ice clouds are the most frequent cloud type over the Antarctic Plateau and are present throughout the year, their optical properties are analyzed with a focus on seasonal variability. Dome C represents an exceptional site for such analysis, as it is characterized by pronounced variations in thermodynamic conditions and atmospheric dynamics. Table 5 reports the seasonal median \pm MAD values for the retrieved properties of ice clouds: τ , $\langle T_{\text{cloud}} \rangle$, and $\langle D_{\text{eff, ice}} \rangle$. The results show that, in summer, ice clouds are found at warmer layers and present smaller optical depths with respect to the other seasons. The largest median cloud optical depth is found in winter. Finally, the particle size distribution effective diameter shows lower values during austral summer and autumn, although seasonal differences remain limited.



Table 5. Seasonal median \pm MAD values of τ , $\langle T_{\text{cloud}} \rangle$, and $\langle D_{\text{eff, ice}} \rangle$ for ice clouds.

	DJF	MAM	JJA	SON
τ	0.11 ± 0.05	0.23 ± 0.10	0.32 ± 0.14	0.30 ± 0.15
$\langle T_{\text{cloud}} \rangle$ [K]	242.7 ± 3.2	236.3 ± 3.7	233.6 ± 3.4	236.3 ± 4.4
$\langle D_{\text{eff, ice}} \rangle$ [μm]	22 ± 4	22 ± 4	23 ± 5	24 ± 5
N_{tot}	4260	3291	3178	2782

345 4.2 Mixed-phase clouds

Mixed-phase clouds are observed only in the time-frame from November to March. The retrieved ice contribution has an average value of approximately 0.5, indicating that the total mass of ice is comparable to that of liquid water within the same mixed-phase cloud. Histograms of τ (upper panel), CBH (middle-left panel), $\langle T_{\text{cloud}} \rangle$ (middle-right panel), $\langle D_{\text{eff, ice}} \rangle$ (lower-left panel), and the effective diameter of water droplets $\langle D_{\text{eff, water}} \rangle$ (lower-right panel) are shown in Fig. 9. The average optical
 350 depth of mixed-phase clouds is markedly higher than that of ice clouds; the τ distribution is characterized by a broad peak between 0.6 and 0.8, median value exceeding 1.5, and minimum value larger than 0.35. Mixed-phase clouds are found in significantly warmer atmospheric layers compared to ice clouds, with median temperatures of approximately 246 K. Moreover, their temperature distribution is more tightly clustered around the median and exhibits a sharper peak than ice clouds, as indicated by lower MAD values. Notably, the central 90% of elements of the distribution falls within a relatively narrow
 355 temperature range, spanning from 241 K to 251 K.

The distribution of $\langle D_{\text{eff, water}} \rangle$ indicates a high occurrence of small droplets, with 18% having effective diameters below 5 μm , and presenting a secondary peak around 8 μm .

High-level mixed-phase clouds exhibit a secondary peak around 8 μm which is not observed in low-level clouds. Overall, 95% of droplet diameters fall below 24 μm . The effective diameters of ice particles in mixed-phase clouds are generally smaller
 360 than those in pure ice clouds, with median values around 13 μm .

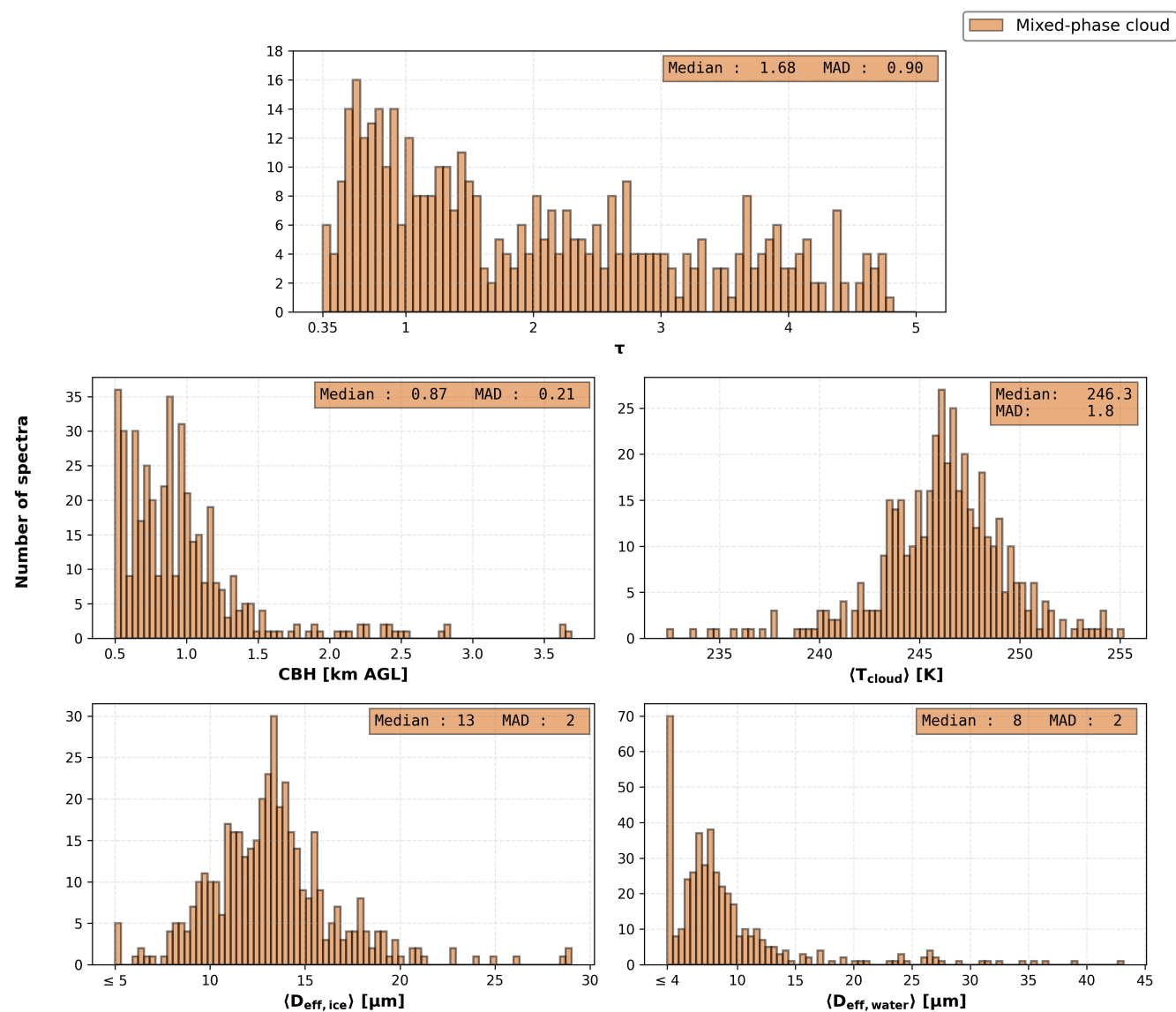


Figure 9. Histograms of mixed-phase cloud properties. The upper panel shows the distribution of optical depth τ . The second row shows the CBH (left panel) and the mean cloud temperature $\langle T_{\text{cloud}} \rangle$ (right panel). The bottom row shows the mean effective dimension of ice crystals $\langle D_{\text{eff, ice}} \rangle$ (left panel) and water droplets' diameters' $\langle D_{\text{eff, water}} \rangle$ (right panel).

4.3 Correlation analysis of cloud properties

Possible correlations among the derived cloud properties and atmospheric parameters such as temperature and altitude are investigated. In Fig. 10, we illustrate the relationship between the binned CBH and $\langle T_{\text{cloud}} \rangle$ (left panel), and between the binned CBH and $\langle D_{\text{eff, ice/water}} \rangle$ (right panel) during the austral summer season (DJF). The CBH is binned in 250m intervals, and for each bin, the median values of temperature and effective dimension are shown, with error bars representing one MAD. Ice clouds are represented with circular markers, while mixed-phase clouds are shown with triangular markers. The figures also include the number of observations for each data point.

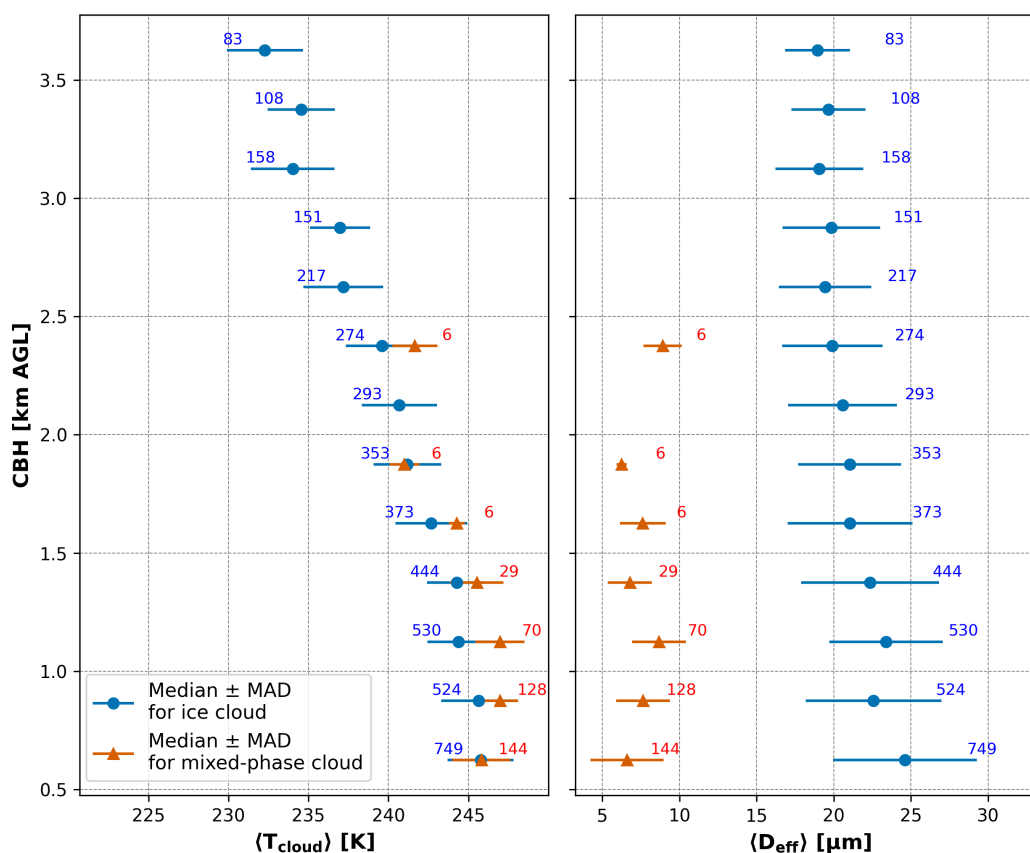


Figure 10. Cloud Base Height as a function of cloud temperature (left panel) and effective dimension of ice crystals/water droplets (right panel) during the DJF season. CBH is binned in 250m intervals. Each marker represents the median within a given height bin, with error bars indicating one MAD. Observation counts for each bin are also reported. Ice clouds are shown with circular markers, mixed-phase clouds with triangular markers.

The results show that, for both ice and mixed-phase clouds, the median cloud temperature increases with altitude in the first (lowest) atmospheric layers, up to approximately 850m AGL where a maximum is reached. Above this level, mean



370 cloud temperature decreases with altitude. Mixed-phase clouds are mostly found at lower altitudes than ice clouds, and, within the same bin of cloud base height, their temperatures are similar to those characterizing ice clouds. For ice clouds, the median effective dimension of the crystals slowly decreases with increasing CBH, as shown in the right panel of Fig. 10. The maximum value, found at the lowest atmospheric level, is approximately $25\mu\text{m}$ while the minimum one is $18\mu\text{m}$ which is reached at the highest level considered, above 3.5 km AGL. No clear trend is observed in the presence of mixed-phase clouds which show a maximum value of the median effective dimension of $9\mu\text{m}$. Similar patterns are observed across all seasons (see Appendix B).

375

The panels of Fig. 11 show the ice cloud τ as a function of $\langle D_{\text{eff, ice}} \rangle$, ice water path (IWP), and $\langle T_{\text{cloud}} \rangle$. The relationships between these variables are quantitatively assessed using the Pearson correlation coefficient (ρ), which measures linear dependence, and the Mutual Information (MI) parameter, which provides a more general measure of statistical dependence, including non-linear relationships. Details on the computation and interpretation of these metrics are provided in Appendix C. As expected, high values of both ρ and MI are found for the relationship between τ and IWP. Accordingly, following Di Natale

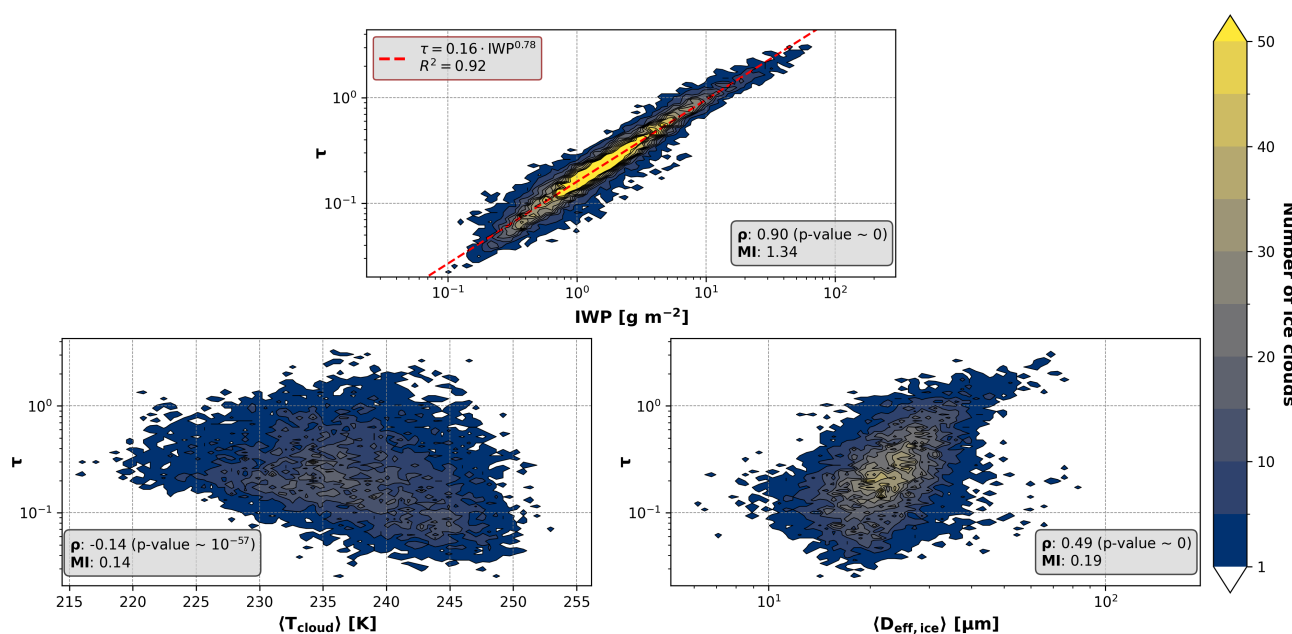


Figure 11. Number density of ice clouds as a function of retrieved cloud optical depth (in logarithmic scale) and ice cloud properties: IWP (upper panel), $\langle T_{\text{cloud}} \rangle$ (lower left panel), and $\langle D_{\text{eff, ice}} \rangle$ (lower right panel). Pearson correlation (ρ) and mutual information (MI) coefficients are also reported. A fitted power law for τ as a function of IWP is displayed with a dotted line in the upper panel.

380

et al. (2020a), τ is fitted as a power law of the form $\tau = a \cdot \text{IWP}^b$. The resulting fit, together with the associated coefficients of determination (R^2), are shown in the corresponding panels of the figure. The estimated parameters a and b are comparable to those reported by Di Natale et al. (2020a), who analyzed a limited subset of the REFIR-PAD dataset. Moderately high values



of the ρ and MI coefficients are also found for the optical depth relationship with $\langle D_{\text{eff, ice}} \rangle$. Finally, the cloud temperature
 385 $\langle T_{\text{cloud}} \rangle$ shows a very weak, yet statistically significant, negative linear correlation with τ . Note that the MI still yields moderate, non-zero values, suggesting that the two variables are dependent, not through a linear relationship but rather through a more complex form of association.

5 Parameterization of ice clouds effective dimensions

A parameterization for the bulk dimension of Antarctic ice clouds as a function of $\langle T_{\text{cloud}} \rangle$ and the mean ice water content
 390 (IWC) is proposed. The parametrization aims at characterizing ice clouds with CBH higher than 500m. For its computation we consider only the cases for which collocated lidar observations are available. The definition of effective dimension of ice clouds follows the one reported in Yang et al. (2005):

$$D_{\text{eff, ice}} = \frac{3 \int_{L_{\text{min}}}^{L_{\text{max}}} \sum_h f_h V_h(L) n(L) dL}{2 \int_{L_{\text{min}}}^{L_{\text{max}}} \sum_h f_h A_h(L) n(L) dL}, \quad (6)$$

where h refers to the ice crystal habit, f_h is the fraction of each habit such that $\sum_h f_h = 1$, L is the maximum dimension of
 395 the ice crystals, $A_h(L)$ and $V_h(L)$ are, respectively, the projected area and volume of the ice crystal, and $n(L)$ is the particle size distribution. Since in the SACR model the ice distribution along the cloud vertical extent is assumed constant, the IWC is estimated as the ratio between the ice water path (IWP) and the cloud geometrical thickness (ΔCH):

$$\text{IWC} = \frac{\text{IWP}}{\Delta\text{CH}} = \frac{\text{IWP}}{\text{CTH} - \text{CBH}} \quad (7)$$

The functional form of the parameterization is assumed to be:

$$400 \langle D_{\text{eff, ice}} \rangle = a + b \cdot \log_{10}(\text{IWC}) + c \cdot [\log_{10}(\text{IWC})]^2 + d \cdot \langle T_{\text{cloud}} \rangle + e \cdot \log_{10}(\text{IWC}) \cdot \langle T_{\text{cloud}} \rangle \quad (8)$$

The above relation is selected among a set of tested functional forms that account for multiple combinations of the terms $\log_{10}(\text{IWC})$ and $\langle T_{\text{cloud}} \rangle$. The parameters are fitted using the ordinary least squares method. Table 6 summarizes the resulting values, along with the temperature and IWC ranges over which the parameterization is valid.

Table 6. Fitted parameters for the ice cloud effective diameter parameterization, along with the corresponding temperature and IWC validity ranges.

a	b	c	d	e	$[T_{\text{cloud}}^{\text{min}}, T_{\text{cloud}}^{\text{max}}]$ [K]	$[\text{IWC}^{\text{min}}, \text{IWC}^{\text{max}}]$ [$g\ m^{-3}$]
-280.1 ± 21.4	-82.2 ± 9.6	2.8 ± 0.3	1.4 ± 0.1	0.43 ± 0.04	[221.3, 249.6]	$[8.10 \cdot 10^{-4}, 5.8 \cdot 10^{-2}]$

In Fig. 12 the parameterized effective dimensions are plotted, with all the retrieved values of $\langle D_{\text{eff, ice}} \rangle$. Each parameterization
 405 is plotted as a function of one predictor variable at a time: $\langle T_{\text{cloud}} \rangle$ in the left panel, and IWC in the right one. In each subplot,

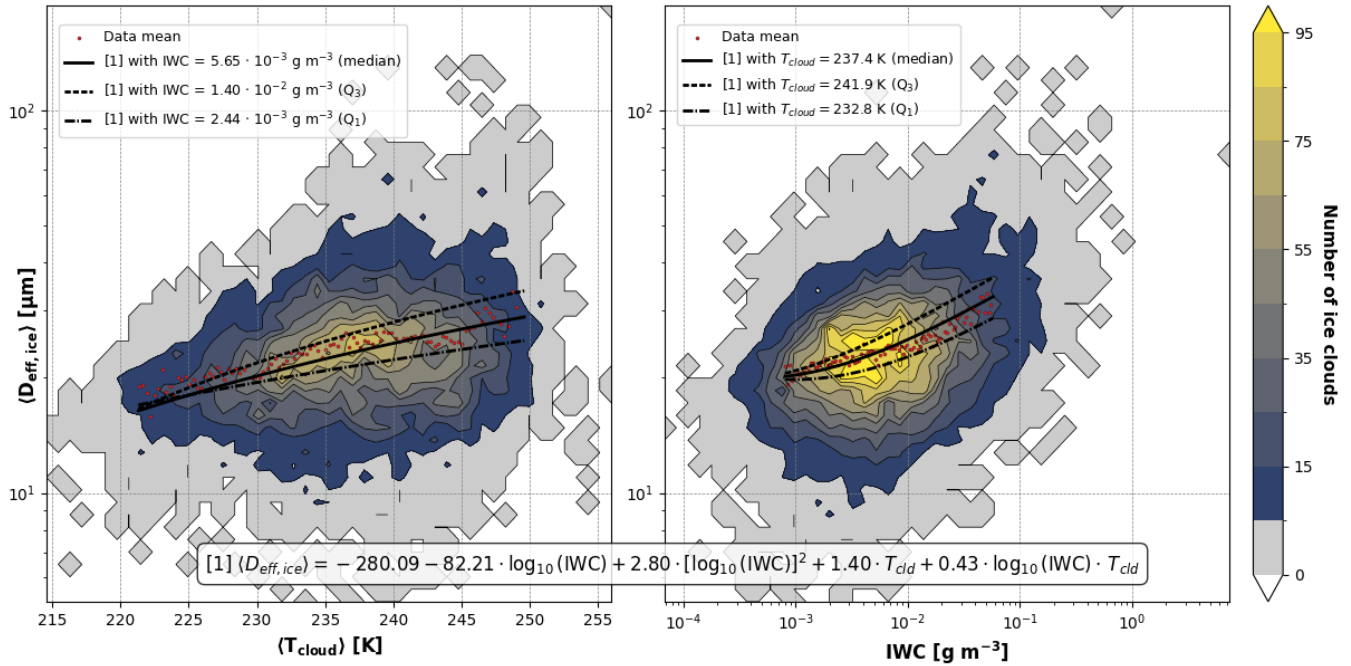


Figure 12. $\langle D_{\text{eff, ice}} \rangle$ as a function of $\langle T_{\text{cloud}} \rangle$ (left panel) and IWC (right panel). Curves indicate the parameterization evaluated at fixed values of $\langle T_{\text{cloud}} \rangle$ and IWC. Markers refer to the mean values from the data.

the remaining variable is held fixed at representative values corresponding to the median and the first and third quartiles (Q_1 and Q_3) of its distribution in the dataset.

To assess the goodness of the parameterization, the root mean square error (RMSE), mean absolute error (MAE), bias, and R^2 are computed. The results are reported in Table 7. The parameterization performs very well as indicated by the low values of the bias in comparison with the typical particle dimensions, meaning that the deviations are predominantly random rather than systematic. The relatively low coefficient of determination reflects the intrinsic variability of ice cloud microphysical properties, as well as the uncertainties associated with remote-sensing retrievals. This suggests that, while temperature and ice water content capture part of the variability in effective dimension, additional factors such as crystal habit variability, microphysical and dynamical processes may also play a significant role. The parameterization captures the central tendency of the observed variability and provides a practical representation for large-scale models, where sub-grid microphysical variability cannot be explicitly resolved.

An analysis of the absolute residuals is provided in Fig. 13. The absolute residual is defined as:

$$\epsilon_a = \langle D_{\text{eff, ice}} \rangle^{\text{observed}} - \langle D_{\text{eff, ice}} \rangle^{\text{predicted}}, \quad (9)$$



Table 7. Statistical evaluation of the parametrization against observations.

RMSE [μm]	MAE [μm]	Bias [μm]	R^2
7.83	5.55	-4.9×10^{-14}	0.29

420 The analysis is performed by examining the distribution of ϵ_a with respect to each predictor variable, binning the data along each one separately. Across all bins, the median residuals remain close to zero, while their variance increases with both $\langle T_{\text{cloud}} \rangle$ and IWC.

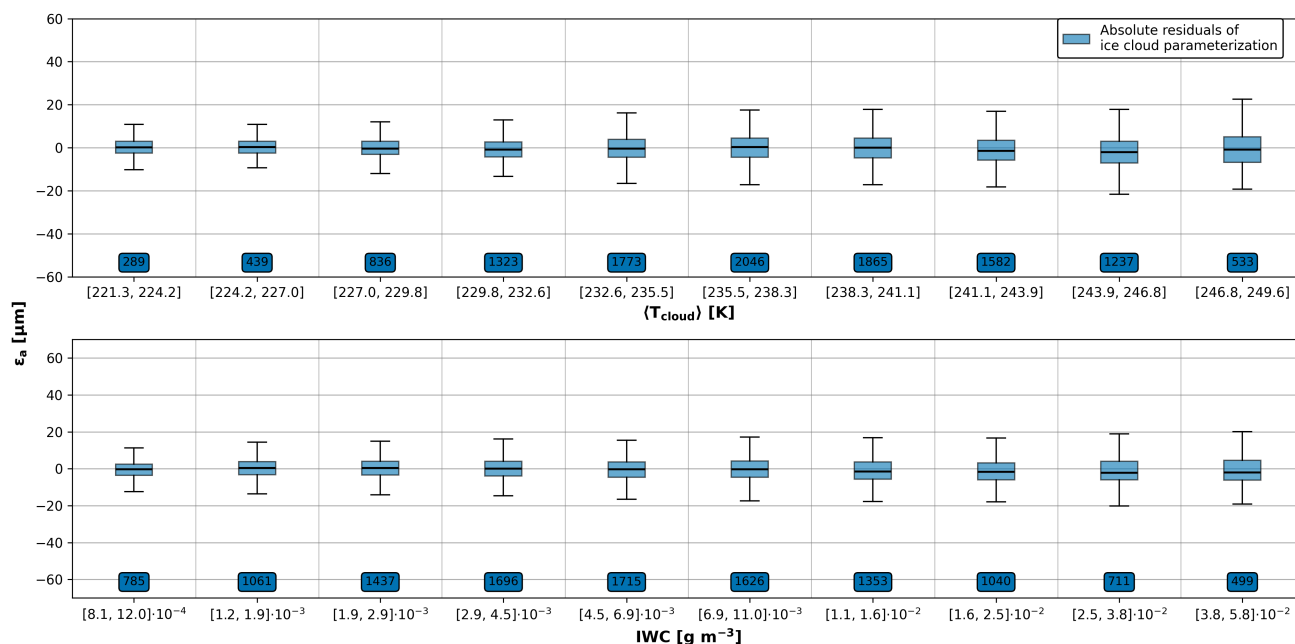


Figure 13. Box plots of the absolute residuals of the parameterizations as a function of $\langle T_{\text{cloud}} \rangle$ (upper panel) and IWC (lower panel), with the number of clouds in each bin indicated at the bottom of each box.

Finally, a qualitative comparison of our ice cloud effective dimension parameterization with those from the literature is performed. Information on the derivation and underlying assumptions of each parameterization are summarized in Tables 8 and 9. For clarity, the square-bracketed identifiers used in the tables (e.g., [P1]) refer to article references listed in Table 8.

425 As shown in Table 9, the various parameterizations are developed using different definitions of effective dimensions, crystal habits, and particle size distributions, which makes a direct comparison not possible. For this reason, each parameterization is converted to the definition of effective size adopted in this study (Eq. (6)), which is consistent with that introduced by Foot (1988). Parameterization [P6] already employs an expression equivalent to the Foot (1988) definition (see Francis et al. (1994)).



Table 8. Reference, data sources and target cloud types for each parameterization.

	Reference	Data Source	Target Cloud Type
[P1]	Ou and Liou (1995)	Heymsfield and Platt (1984)	Mid-latitude cirrus
[P2]	Wyser (1998)	CEPEX, Heymsfield and Platt (1984)	Ice clouds
[P3]	Sun and Rikus (1999)	CEPEX, ICE215, ICE217	Tropical and mid-latitude cirrus
[P4]	Boudala et al. (2002)	BASE, FIRE-ACE, CFDEI, CFDEII	High-latitude stratiform ice clouds
[P5]	McFarquhar et al. (2003)	CEPEX	Tropical anvil clouds
[P6]	Heymsfield et al. (2014)	FIRE-2, CRYSTAL-FACE (CF), PA, SCOUT, ARM 2000 IOP, NAMMA, TC4, AIRS-2, C3VP, MPACE	High-altitude ice clouds

Where:

- CEPEX : Central Equatorial Pacific Experiment
- ICE (215 and 217) : International Cirrus Experiment
- BASE : Beaufort and Arctic Storms Experiment
- FIRE-ACE : Arctic Cloud Experiment
- FIRE-2 : First International Satellite Cloud Climatology Project Regional Experiment
- CFDE (I and II) : Canadian Freezing Drizzle Experiment
- PA : PreAura Validation Experiment
- ARM 2000 IOP : Atmospheric Radiation Measurement 2000 intensive observing period
- TC4 : Tropical Clouds, Convection, Chemistry and Climate
- C3VP : CloudSat/CALIPSO Validation Project
- CRYSTAL-FACE (CF) : Cirrus Regional Study of Tropical Anvils and Cirrus Layers–Florida-Area Cirrus Experiment
- SCOUT : Stratospheric–Climate Links with Emphasis on the Upper Troposphere and Lower Stratosphere
- AIRS-2 : Alliance Icing Research Study II
- NAMMA : NASA African Monsoon Multidisciplinary Analyses
- MPACE : Mixed-Phase Polar Arctic Cloud Experiment

In contrast, parameterizations [P3], [P4], and [P5] use the formulation proposed by Fu (1996), which can be related to the
430 Foot definition through the following conversion formula (Sun and Rikus, 1999):

$$D_{\text{eff}}^{\text{Foot}} = \frac{3\sqrt{3}}{4} D_{\text{eff}}^{\text{Fu}} \quad (10)$$

Finally, parameterizations [P1] and [P2] use their own definitions. However, appropriate normalization factors can be applied
to obtain equivalent expressions, at least in the limiting case where $D = L$. Wyser (1998) showed that such normalizations
improve the agreement between different parameterization schemes. The results of the comparison are shown in Fig. 14, where
435 the various schemes are plotted as functions of $\langle T_{\text{cloud}} \rangle$ and IWC. Wyser (1998), Sun and Rikus (1999), and Boudala et al.
(2002) provide equations that depend on both temperature and IWC, so that, when plotted as a function of one variable,
the other is kept constant at the median of the observed data. In contrast, Heymsfield et al. (2014) and Ou and Liou (1995)
provide schemes depending on temperature only, while the parametrization in McFarquhar et al. (2003) depends solely on
IWC. Figure 14 highlights significant differences among the ice cloud effective dimension parameterizations available in



Table 9. Definitions of effective diameter, particle habits, and particle size distributions (PSD) used for each parameterization.

	Definition of effective size	Habits	PSD
[P1]	$D_{\text{eff}} = \frac{\int_{L_{\min}}^{L_{\max}} D^2 L n(L) dL}{\int_{L_{\min}}^{L_{\max}} D L n(L) dL}$ with $L_{\min} = 20 \mu\text{m}$	Hexagonal	Power law
[P2]	$r_{\text{eff}} = \frac{\int D^2 L n(L) dL}{\int (D^2 L)^{2/3} n(L) dL}$	Hexagonal columns	<ul style="list-style-type: none"> • Γ distribution if $L \leq 20 \mu\text{m}$ • Power law if $L > 20 \mu\text{m}$
[P3]	$D_{\text{eff}} = \frac{\int D^2 L n(L) dL}{\int (DL + \sqrt{3/4} D^2) n(L) dL}$	Regular hexagonal columns	<ul style="list-style-type: none"> • Γ distribution if $D_m < 100 \mu\text{m}$ • Lognormal if $D_m \geq 100 \mu\text{m}$
[P4]	$D_{\text{eff}} = \frac{2\sqrt{3}\text{IWC}}{3\rho A}$	Measured	<ul style="list-style-type: none"> • Γ distribution if $D_M \leq 100 \mu\text{m}$ • Measured if $D_M > 100 \mu\text{m}$
[P5]	$r_{\text{eff}} = \frac{\sqrt{3}\text{IWC}}{3\rho A}$	Measured	<ul style="list-style-type: none"> • Γ distribution if $D_m < 100 \mu\text{m}$ • Measured if $D_m > 100 \mu\text{m}$
[P6]	$D_{\text{eff}} = \frac{3\text{IWC}}{2\rho A}$	Measured	Fitted Γ functions

Where:

- D : ice crystal width
- ρ : density of ice
- L : ice crystal length
- A : cross-sectional area per unit volume
- $n(L)$: particle size distribution
- D_m : diameter of a mass-equivalent sphere
- IWC : ice water content
- D_M : maximum dimension of the ice particle

440 the literature, which is an expected result since they are derived for different sets of cloud types. The differences also arise partly from the assumptions regarding ice particle habits and particle size distributions. Overall, literature parameterizations tend to overestimate the effective dimension of Antarctic ice crystals compared to the values retrieved in this study for high clouds. Among the parameterizations considered, Boudala et al. (2002) shows the closest agreement with our results. This is consistent with the fact that it was developed specifically for high-latitude ice clouds, with all datasets collected at latitudes above 45°N , thus considering atmospheric conditions somehow similar to those investigated here. It is worth noting that all the 445 parameterizations shown in Fig. 14 are based on in situ measurements (see Table 8), whereas the parameterization developed in this study relies exclusively on remote-sensing observations.

The systematic differences identified in ice crystal effective dimension relative to commonly used parameterizations imply potential biases in the representation of cloud radiative effects in models. In particular, smaller effective dimensions are expected to enhance cloud optical thickness and modify both long-wave and short-wave radiative fluxes, suggesting that the use 450 of non-Antarctic parameterizations may lead to inaccuracies in simulated surface energy budgets over the Antarctic Plateau.

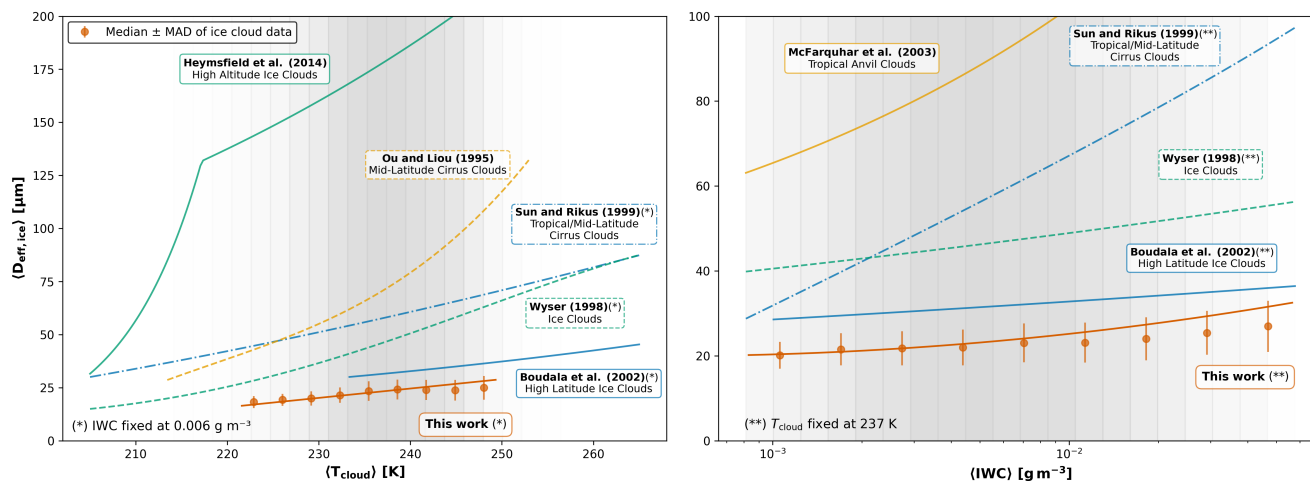


Figure 14. The parameterization developed in this study is compared with parameterizations from the literature. Observations are displayed as markers (medians), with error bars indicating the MAD. The vertical grey shaded bands in the background represent the density of observed clouds, with darker shading indicating higher occurrence. Left panel: $\langle D_{\text{eff, ice}} \rangle$ as a function of $\langle T_{\text{cloud}} \rangle$. Parameterizations that additionally depend on IWC, including that developed in this study, are shown for a fixed IWC of $6 \times 10^{-3} \text{ gm}^{-3}$. Right panel: same as the left panel, but showing $\langle D_{\text{eff, ice}} \rangle$ as a function of IWC. Temperature is fixed at 237 K.

6 Conclusions

This study provides a comprehensive observational characterization of cloud occurrence and properties over the Antarctic Plateau, based on nine years of ground-based far-infrared and mid-infrared spectral measurements from the REFIR-PAD instrument at Dome C, combined with co-located lidar observations. The application of the updated machine-learning algorithm CIC to REFIR-PAD radiance spectra enables the classification of sky conditions into three categories (clear sky, ice clouds, and mixed-phase clouds), a distinction that is particularly challenging to achieve using satellite observations alone. Results confirm that clear sky conditions dominate the Antarctic Plateau, occurring in $67.7 \pm 1.3\%$ of all observations. Ice clouds account for most cloudy scenes, while mixed-phase clouds appear almost exclusively during the austral summer, representing approximately 22.8% of total cloudiness in that season. These results consolidate preliminary findings reported in earlier works (Ricaud et al., 2024a; Cossich et al., 2021). Cloud presence is systematically associated with warmer surface temperatures in all seasons. The classified spectra are subsequently processed by the SACR retrieval algorithm to derive the optical and microphysical properties of the clouds. The retrieved parameters highlight distinct differences among cloud types and vertical regimes. Ice clouds over Dome C are predominantly optically thin, with the majority of cases exhibiting optical depths below 1 and with a median effective diameter of $23 \mu\text{m}$. The retrieved dimensions are comparable to those reported in previous studies accounting for ground-based retrievals at Dome C (e.g. Maestri et al. (2019a)), while significantly smaller than those obtained in Arctic and midlatitude cirri by in-situ observations (Järvinen and Schnaiter, 2026).



In contrast, mixed-phase clouds are optically thicker, with median optical depths exceeding 1.5, are characterized by warmer temperatures, and largely confined to the lowest layers of the atmosphere.

470 A key outcome of this work is the development of a new parameterization of ice crystal effective dimension as a function of cloud temperature and ice water content. This parameterization, derived from long-term remote-sensing observations, differs significantly from existing schemes which have been mostly developed for midlatitude and non-Antarctic environments. All the tested schemes overestimate our findings on ice crystal effective dimensions. The parameterization from Boudala et al. (2002), development for high-latitude conditions, shows the closest agreement.

475 Since ice particle sizes directly influence cloud optical properties and radiative fluxes, the adoption of inaccurate dimension parameterization might introduce systematic biases in cloud radiative effects, surface energy budget and ultimately climate projections. Therefore, the use of a region-specific parameterization, such as the one proposed here, represents a step toward improving the representation of cloud–radiation interactions in atmospheric models, potentially reducing uncertainties in the simulation of Antarctic climate.

480 However, it should be noted that the present analysis is necessarily limited to the conditions observed at Dome C, and the applicability of the results to other Antarctic regions should be further investigated. Additionally, uncertainties related to remote sensing retrievals could be minimized by the use of in-situ information providing direct measurements of the particle size distributions and the identification of the particle shapes. Future work should address these limitations by (i) validating the retrieved properties against in-situ measurements, (ii) quantifying the radiative impact of the retrieved microphysical properties
485 through dedicated radiative transfer experiments and simulations in climate and NWP models, and (iii) extending the analysis to synergistic satellite observations to assess spatial representativeness beyond Dome C.

Overall, this study provides new observational constraints on Antarctic cloud microphysics and highlights the need for region-specific parameterizations to improve the representation of cloud–radiation interactions in atmospheric models.

Code availability. The CIC source code used in this study is currently being prepared for public release and will be archived on Zenodo
490 upon publication of this article.

Data availability. The Antarctic lidar data are reachable at <http://lidarmax.altervista.org/englidar/Antarctic%20LIDAR.php> (last access: 27 April 2026). Radiosondes and meteorological data are available at <http://www.climantartide.it> (last access: 27 April 2026). Radiance spectra are available on request to INO-CNR personnel (GDN and LP).



Appendix A: Frequency of occurrence of ice and mixed-phase clouds

495 Figures A1 and A2 show the seasonal and interannual relative frequency of ice and mixed-phase clouds, respectively, for cases with lidar-retrieved CBH below and above 500 m AGL, excluding observations from 2012–2013 to avoid biases due to limited and uneven data coverage. In general, cloud cases with CBH below 500 m AGL, thus excluded from the retrieval of cloud properties, represent the majority of observations, particularly for mixed-phase clouds. For ice clouds, a seasonal variability is observed: the austral Summer consistently shows the highest relative frequency of clouds with CBH above the 500 m threshold. In contrast, the relative frequency of clouds below the threshold reaches its maximum during the austral Winter or Spring.

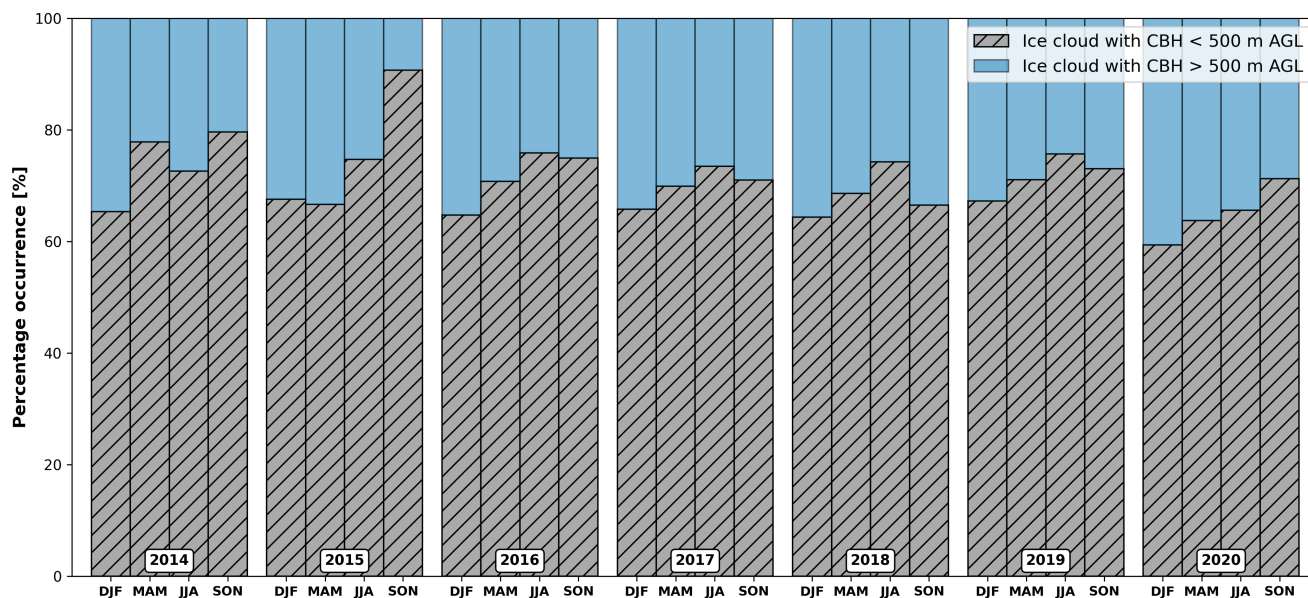


Figure A1. Seasonal and interannual relative occurrence of ice clouds with CBH below and above 500 m AGL (2014–2020).

500

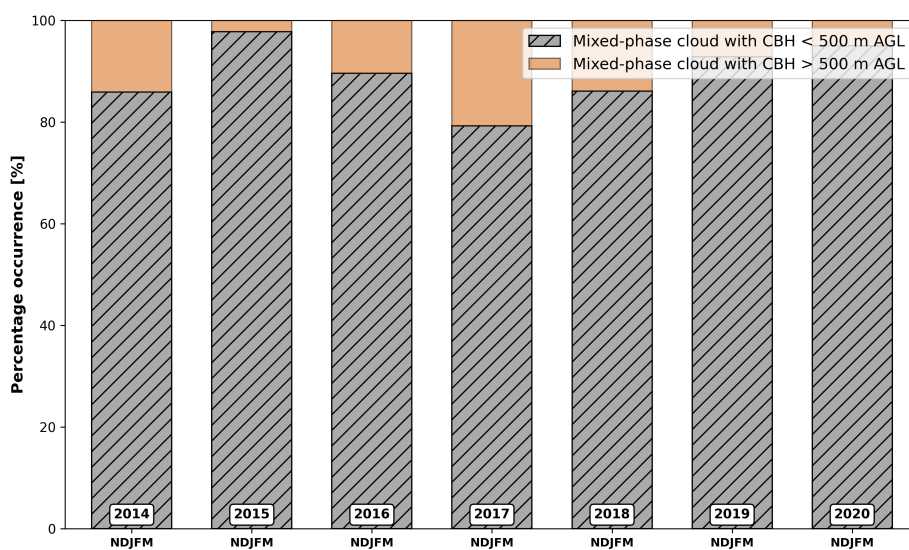


Figure A2. Seasonal and interannual relative occurrence of mixed-phase clouds with CBH below and above 500 m AGL (2014–2020).

<https://doi.org/10.5194/egusphere-2026-2806>

Preprint. Discussion started: 23 June 2026

© Author(s) 2026. CC BY 4.0 License.



Appendix B: Correlation analysis of cloud properties

Possible correlations among the derived cloud properties (mean temperature, cloud base height, effective dimension) for Autumn, Winter and Spring.

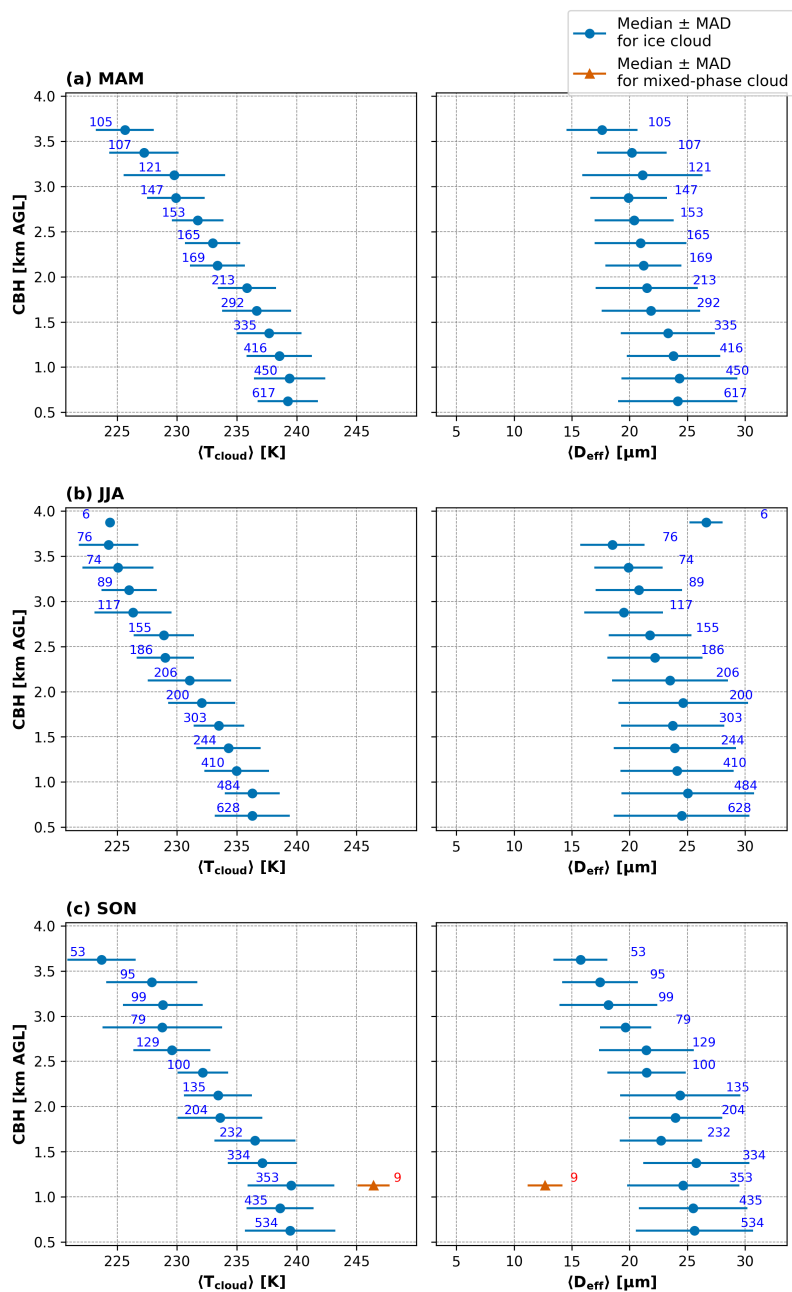


Figure B1. Cloud bottom height as a function of cloud temperature (left panels) and effective dimension of ice crystals/water droplets (right panels) for the MAM (a), JJA (b), and SON (c) seasons. Cloud bottom height is binned in 250 m intervals. Each marker represents the median within a given height bin, with error bars indicating one median absolute deviation (MAD). Observation counts for each bin are also reported.



Appendix C: Pearson correlation and mutual information

505 The Pearson correlation coefficient measures the strength and direction of the linear relationship between two random variables X and Y , and is defined as:

$$\rho_{X,Y} = \frac{\text{cov}(X,Y)}{\sigma_X \sigma_Y} = \frac{E[(X - \mu_X)(Y - \mu_Y)]}{\sigma_X \sigma_Y} \quad (\text{C1})$$

where μ_X and μ_Y are the means of X and Y , respectively, σ_X and σ_Y are their standard deviations and $\text{cov}(X,Y)$ is their covariance. The coefficient ρ ranges from -1 (perfect negative linear correlation) to $+1$ (perfect positive linear correlation), with $\rho = 0$ indicating that there is no linear relationship between the variables. The associated p-value is used to assess the statistical significance of the computed value ρ . In fact, it represents the probability of observing a correlation coefficient at least as extreme as the one calculated from the data, under the null hypothesis of no correlation (i.e. $\rho = 0$). The Mutual Information (MI), instead, quantifies how much information one variable contains about the other, regardless of the nature of their relationship. It is defined as:

$$515 \quad \text{MI} = \sum_{x \in X} \sum_{y \in Y} p(x,y) \log \left(\frac{p(x,y)}{p(x)p(y)} \right) \quad (\text{C2})$$

where $p(x)$ and $p(y)$ represent the marginal probabilities of the two random variables, and $p(x,y)$ is their joint probability. It can also be defined in terms of entropy as:

$$\text{MI}(X;Y) = H(X) - H(X|Y) \quad (\text{C3})$$

where $H(X)$ is the entropy of X , and $H(X|Y)$ is the entropy of X conditioned on Y . The MI coefficient is always non-negative, with $\text{MI} = 0$ indicating that the variables are independent.

The choice of these two statistical measures is motivated by their ability to describe complementary aspects of the association between two random variables. The Pearson correlation coefficient quantifies only linear dependence; therefore, a value of $\rho = 0$ does not necessarily imply statistical independence, but rather the absence of a linear relationship (for example, if $Y = X^2$, the value of ρ is zero). In contrast, Mutual Information provides a more general measure of dependence, capturing both linear and non-linear relationships between variables.

<https://doi.org/10.5194/egusphere-2026-2806>

Preprint. Discussion started: 23 June 2026

© Author(s) 2026. CC BY 4.0 License.



Author contributions. Conceptualization:TM, EF. Formal Analysis: EF, GDN. Methodology: TM, EF, GDN, FD. Investigation: EF, TM. Data Curation: GB, MDG. Software: EF, GDN, MM. Visualization: EF. Funding acquisition: GDN, TM, LP. Supervision: TM. Writing – original draft: EF, TM. Writing – review and editing: EF, TM, MM, FD, GB, MDG, LP, GM, GL, TR, PY

Competing interests. The authors declare that they have no known competing financial interests or personal relationships that could have
530 appeared to influence the work reported in this paper.

Acknowledgements. The authors acknowledge the Antarctic Meteo-Climatological Observatory at Concordia for the meteorological data availability.



References

- Adhikari, L., Wang, Z., and Deng, M.: Seasonal variations of Antarctic clouds observed by CloudSat and CALIPSO satellites, *J. Geophys. Res. Atmos.*, 117, D04 202, <https://doi.org/10.1029/2011JD016719>, 2012.
- Bertossa, C., L'Ecuyer, T., Merrelli, A., Huang, X., and Chen, X.: A Neural Network–Based Cloud Mask for PREFIRE and Evaluation with Simulated Observations, *J. Atmos. Ocean. Technol.*, 40, 377 – 396, <https://doi.org/10.1175/JTECH-D-22-0023.1>, 2023.
- Bianchini, G., Castagnoli, F., Di Natale, G., and Palchetti, L.: A Fourier transform spectroradiometer for ground-based remote sensing of the atmospheric downwelling long-wave radiance, *Atmos. Meas. Tech.*, 12, 619–635, <https://doi.org/10.5194/amt-12-619-2019>, 2019.
- 540 Boudala, F. S., Isaac, G. A., Fu, Q., and Cober, S. G.: Parameterization of effective ice particle size for high-latitude clouds, *Int. J. Climatol.*, 22, 1267–1284, <https://doi.org/10.1002/joc.774>, 2002.
- Bozzo, A., Maestri, T., Rizzi, R., and Tosi, E.: Parameterization of single scattering properties of mid-latitude cirrus clouds for fast radiative transfer models using particle mixtures, *Geophys. Res. Lett.*, 35, <https://doi.org/https://doi.org/10.1029/2008GL034695>, 2008.
- Bromwich, D. H., Nicolas, J. P., Hines, K. M., Kay, J. E., Key, E. L., Lazzara, M. A., Lubin, D., McFarquhar, G. M., Gorodetskaya, I. V., Grosvenor, D. P., Lachlan-Cope, T., and van Lipzig, N. P. M.: Tropospheric clouds in Antarctica, *Rev. Geophys.*, 50, RG1004, <https://doi.org/10.1029/2011RG000363>, 2012.
- Chan, M. A. and Comiso, J. C.: Cloud features detected by MODIS but not by CloudSat and CALIOP, *Geophys. Res. Lett.*, 38, L24 813, <https://doi.org/10.1029/2011GL050063>, 2011.
- Cossich, W., Maestri, T., Magurno, D., Martinazzo, M., Di Natale, G., Palchetti, L., Bianchini, G., and Del Guasta, M.: Ice and mixed-phase cloud statistics on the Antarctic Plateau, *Atmos. Chem. Phys.*, 21, 13 811–13 833, <https://doi.org/10.5194/acp-21-13811-2021>, 2021.
- 550 Di Natale, G., Bianchini, G., Del Guasta, M., Ridolfi, M., Maestri, T., Cossich, W., Magurno, D., and Palchetti, L.: Characterization of the Far Infrared Properties and Radiative Forcing of Antarctic Ice and Water Clouds Exploiting the Spectrometer-LiDAR Synergy, *Remote Sens.*, 12, 3574, <https://doi.org/10.3390/rs12213574>, 2020a.
- Di Natale, G., Palchetti, L., Bianchini, G., and Ridolfi, M.: The two-stream δ -Eddington approximation to simulate the Far In-
fraRed Earth spectrum for the Simultaneous Atmospheric and Cloud Retrieval, *J. Quant. Spectrosc. Radiat. Transf.*, 246, 106 927, <https://doi.org/10.1016/j.jqsrt.2020.106927>, 2020b.
- 555 Di Natale, G., Turner, D. D., Bianchini, G., Del Guasta, M., Palchetti, L., Bracci, A., Baldini, L., Maestri, T., Cossich, W., Martinazzo, M., and Facheris, L.: Consistency test of precipitating ice cloud retrieval properties obtained from the observations of different instruments operating at Dome C (Antarctica), *Atmos. Meas. Tech.*, 15, 7235–7258, <https://doi.org/10.5194/amt-15-7235-2022>, 2022.
- 560 Donat, F., Fabbri, E., Maestri, T., Martinazzo, M., Masin, F., Pelliccia, G. P., Cassini, L., Masiello, G., Liuzzi, G., and Serio, C.: The cloud identification and classification (CIC) algorithm for high spectral resolution observations in the far- and mid-infrared part of the spectrum, in: Proceedings Volume 13193, Remote Sensing of Clouds and the Atmosphere XXIX, Edinburgh, United Kingdom, 20 November 2024, p. 1319302, <https://doi.org/10.1117/12.3031709>, 2024.
- 565 Donat, F., Maestri, T., Fabbri, E., Martinazzo, M., Bianchini, G., Del Guasta, M., Di Natale, G., Palchetti, L., Masiello, G., Serio, C., and Liuzzi, G.: Ground-based detection of Antarctic clouds: analysis of cycles and comparison with IASI products, *EGUsphere [preprint]*, <https://doi.org/10.5194/egusphere-2025-2793>, 2025.
- D'Alessandro, J. J. and McFarquhar, G. M.: Impacts of Drop Clustering and Entrainment-Mixing on Mixed Phase Shallow Cloud Properties Over the Southern Ocean: Results From SOCRATES, *J. Geophys. Res. Atmos.*, 128, e2023JD038 622, <https://doi.org/10.1029/2023JD038622>, e2023JD038622 2023JD038622, 2023.



- 570 Foot, J. S.: Some observations of the optical properties of clouds. II: Cirrus, *Q. J. R. Meteorol. Soc.*, 114, 145–164, <https://doi.org/10.1002/qj.49711447908>, 1988.
- Francis, P. N., Jones, A., Saunders, R. W., Shine, K. P., Slingo, A., and Sun, Z.: An observational and theoretical study of the radiative properties of cirrus: Some results from ICE'89, *Q. J. R. Meteorol. Soc.*, 120, 809–848, <https://doi.org/10.1002/qj.49712051804>, 1994.
- Fu, Q.: An Accurate Parameterization of the Solar Radiative Properties of Cirrus Clouds for Climate Models, *J. Clim.*, 9, 2058 – 2082, [https://doi.org/10.1175/1520-0442\(1996\)009<2058:AAPOTS>2.0.CO;2](https://doi.org/10.1175/1520-0442(1996)009<2058:AAPOTS>2.0.CO;2), 1996.
- 575 Guyot, A., Protat, A., Alexander, S. P., Klekociuk, A. R., Kuma, P., and McDonald, A.: Detection of supercooled liquid water containing clouds with ceilometers: development and evaluation of deterministic and data-driven retrievals, *Atmos. Meas. Tech.*, 15, 3663–3681, <https://doi.org/10.5194/amt-15-3663-2022>, 2022.
- Heymsfield, A., Winker, D., Avery, M., Vaughan, M., Diskin, G., Deng, M., Mitev, V., and Matthey, R.: Relationships between Ice Water Content and Volume Extinction Coefficient from In Situ Observations for Temperatures from 0° to -86°C: Implications for Spaceborne Lidar Retrievals, *J. Appl. Meteorol. Climatol.*, 53, 479 – 505, <https://doi.org/10.1175/JAMC-D-13-087.1>, 2014.
- 580 Heymsfield, A. J. and Platt, C. M. R.: A Parameterization of the Particle Size Spectrum of Ice Clouds in Terms of the Ambient Temperature and the Ice Water Content, *J. Atmos. Sci.*, 41, 846 – 855, [https://doi.org/10.1175/1520-0469\(1984\)041<0846:APOTPS>2.0.CO;2](https://doi.org/10.1175/1520-0469(1984)041<0846:APOTPS>2.0.CO;2), 1984.
- INO-CNR Istituto Nazionale di Ottica: <http://lidarmax.altervista.org/englidar/Antarctic%20LIDAR.php>, last access: 14 August 2024.
- 585 Järvinen, E. and Schnaiter, F. M.: Low and consistent asymmetry parameters in Arctic and mid-latitude cirrus, *Atmos. Chem. Phys.*, 26, 2465–2486, <https://doi.org/10.5194/acp-26-2465-2026>, 2026.
- Lachlan-Cope, T.: Antarctic clouds, *Polar Res.*, 29, 150–158, <https://doi.org/10.1111/j.1751-8369.2010.00148.x>, 2010.
- Levenberg, K.: A Method for the Solution of Certain Non-Linear Problems in Least Squares, *Q. Appl. Math.*, 2, 164–168, <https://doi.org/10.1090/qam/10666>, 1944.
- 590 Lubin, D., Chen, B., Bromwich, D. H., Somerville, R. C. J., Lee, W.-H., and Hines, K. M.: The Impact of Antarctic Cloud Radiative Properties on a GCM Climate Simulation, *J. Clim.*, 11, 447 – 462, [https://doi.org/10.1175/1520-0442\(1998\)011<0447:TIOACR>2.0.CO;2](https://doi.org/10.1175/1520-0442(1998)011<0447:TIOACR>2.0.CO;2), 1998.
- Lubin, D., Zhang, D., Silber, I., Scott, R. C., Kalogeras, P., Battaglia, A., Bromwich, D. H., Cadeddu, M., Eloranta, E., Fridlind, A., Frossard, A., Hines, K. M., Kneifel, S., Leaitch, W. R., Lin, W., Nicolas, J., Powers, H., Quinn, P. K., Rowe, P., Russell, L. M., Sharma, S., Verlinde, J., and Vogelmann, A. M.: AWARE: The Atmospheric Radiation Measurement (ARM) West Antarctic Radiation Experiment, *Bull. Amer. Meteor. Soc.*, 101, E1069 – E1091, <https://doi.org/10.1175/BAMS-D-18-0278.1>, 2020.
- 595 Maestri, T., Arosio, C., Rizzi, R., Palchetti, L., Bianchini, G., and Del Guasta, M.: Antarctic Ice Cloud Identification and Properties Using Downwelling Spectral Radiance From 100 to 1,400 cm^{-1} , *J. Geophys. Res. Atmos.*, 124, 4761–4781, <https://doi.org/10.1029/2018JD029205>, 2019a.
- Maestri, T., Cossich, W., and Sbrolli, I.: Cloud identification and classification from high spectral resolution data in the far infrared and mid-infrared, *Atmos. Meas. Tech.*, 12, 3521–3540, <https://doi.org/10.5194/amt-12-3521-2019>, 2019b.
- 600 Magurno, D., Cossich, W., Maestri, T., Bantges, R., Brindley, H., Fox, S., Harlow, C., Murray, J., Pickering, J., Warwick, L., and Oetjen, H.: Cirrus Cloud Identification from Airborne Far-Infrared and Mid-Infrared Spectra, *Remote Sens.*, 12, 2097, <https://doi.org/10.3390/rs12132097>, 2020.
- Malinowski, E. R.: Factor Analysis in Chemistry, *J. Chemometrics*, 16, 635–635, <https://doi.org/10.1002/cem.757>, 2002.
- 605 McFarquhar, G. M. and Heymsfield, A. J.: Parameterization of Tropical Cirrus Ice Crystal Size Distributions and Implications for Radiative Transfer: Results from CEPEX, *J. Atmos. Sci.*, 54, 2187 – 2200, [https://doi.org/10.1175/1520-0469\(1997\)054<2187:POTCIC>2.0.CO;2](https://doi.org/10.1175/1520-0469(1997)054<2187:POTCIC>2.0.CO;2), 1997.



- McFarquhar, G. M., Iacobellis, S., and Somerville, R. C. J.: SCM Simulations of Tropical Ice Clouds Using Observationally Based Parameterizations of Microphysics, *J. Clim.*, 16, 1643 – 1664, [https://doi.org/10.1175/1520-0442\(2003\)016<1643:SSOTIC>2.0.CO;2](https://doi.org/10.1175/1520-0442(2003)016<1643:SSOTIC>2.0.CO;2), 2003.
- 610 Muskatel, H. B., Blahak, U., Khain, P., Levi, Y., and Fu, Q.: Parametrizations of Liquid and Ice Clouds' Optical Properties in Operational Numerical Weather Prediction Models, *Atmos.*, 12, 89, <https://doi.org/10.3390/atmos12010089>, 2021.
- Osservatorio Meteo-Climatologico Antartico: <https://www.climantartide.it>, last access: 14 August 2024.
- Ou, S. and Liou, K.: Ice microphysics and climatic temperature feedback, *Atmos. Res.*, 35, 127–138, [https://doi.org/10.1016/0169-8095\(94\)00014-5](https://doi.org/10.1016/0169-8095(94)00014-5), 1995.
- 615 Palchetti, L., Bianchini, G., Di Natale, G., and Guasta, M.: Far-Infrared Radiative Properties of Water Vapor and Clouds in Antarctica, *Bull. Amer. Meteor. Soc.*, 96, 1505–1518, <https://doi.org/10.1175/BAMS-D-13-00286.1>, 2015.
- Palchetti, L., Brindley, H., Bantges, R., Buehler, S. A., Camy-Peyret, C., Carli, B., Cortesi, U., Bianco, S. D., Natale, G. D., Dinelli, B. M., Feldman, D., Huang, X. L., C.-Labonnote, L., Libois, Q., Maestri, T., Mlynczak, M. G., Murray, J. E., Oetjen, H., Ridolfi, M., Riese, M., Russell, J., Saunders, R., and Serio, C.: FORUM: Unique Far-Infrared Satellite Observations to Better Understand How Earth Radiates
- 620 Energy to Space, *Bull. Amer. Meteor. Soc.*, 101, E2030 – E2046, <https://doi.org/10.1175/BAMS-D-19-0322.1>, 2020.
- Ricaud, P., Del Guasta, M., Lupi, A., Roehrig, R., Bazile, E., Durand, P., Attié, J.-L., Nicosia, A., and Grigioni, P.: Supercooled liquid water clouds observed over Dome C, Antarctica: temperature sensitivity and cloud radiative forcing, *Atmos. Chem. Phys.*, 24, 613–630, <https://doi.org/10.5194/acp-24-613-2024>, 2024a.
- Ricaud, P., Durand, P., Grigioni, P., Del Guasta, M., Camporeale, G., Roy, A., Attié, J.-L., and Bognar, J.: In situ observations of supercooled
- 625 liquid water clouds over Dome C, Antarctica, by balloon-borne sondes, *Atmos. Meas. Tech.*, 17, 5071–5089, <https://doi.org/10.5194/amt-17-5071-2024>, 2024b.
- Sgheri, L., Belotti, C., Ben-Yami, M., Bianchini, G., Carnicero Dominguez, B., Cortesi, U., Cossich, W., Del Bianco, S., Di Natale, G., Guardabrazo, T., Lajas, D., Maestri, T., Magurno, D., Oetjen, H., Raspollini, P., and Sgattoni, C.: The FORUM end-to-end simulator project: architecture and results, *Atmos. Meas. Tech.*, 15, 573–604, <https://doi.org/10.5194/amt-15-573-2022>, 2022.
- 630 Sun, Z. and Rikus, L.: Parametrization of effective sizes of cirrus-cloud particles and its verification against observations, *Q. J. R. Meteorol. Soc.*, 125, 3037–3055, <https://doi.org/10.1002/qj.49712556012>, 1999.
- Turner, D. D., Knuteson, R. O., Revercomb, H. E., Lo, C., and Dedecker, R. G.: Noise Reduction of Atmospheric Emitted Radiation Interferometer (AERI) Observations Using Principal Component Analysis, *J. Atmos. Ocean. Technol.*, 23, 1223 – 1238, <https://doi.org/10.1175/JTECH1906.1>, 2006.
- 635 Van Tricht, K., Gorodetskaya, I. V., Lhermitte, S., Turner, D. D., Schween, J. H., and Van Lipzig, N. P. M.: An improved algorithm for polar cloud-base detection by ceilometer over the ice sheets, *Atmos. Meas. Tech.*, 7, 1153–1167, <https://doi.org/10.5194/amt-7-1153-2014>, 2014.
- Weverberg, K. V., Vogelmann, A. M., Lin, W., Luke, E. P., Cialella, A., Minnis, P., Khaiyer, M., Boer, E. R., and Jensen, M. P.: The Role of Cloud Microphysics Parameterization in the Simulation of Mesoscale Convective System Clouds and Precipitation in the Tropical Western
- 640 Pacific, *J. Atmos. Sci.*, 70, 1104 – 1128, <https://doi.org/10.1175/JAS-D-12-0104.1>, 2013.
- Wyser, K.: The Effective Radius in Ice Clouds, *J. Clim.*, 11, 1793–1802, [https://doi.org/10.1175/1520-0442\(1998\)011<1793:TERIIC>2.0.CO;2](https://doi.org/10.1175/1520-0442(1998)011<1793:TERIIC>2.0.CO;2), 1998.
- Xu, J., Yang, J., Du, Z., Chen, J., Wu, Z., and Xiao, C.: Characteristics of atmospheric ice nucleating particles over East Antarctica retrieved from the surface snow, *Sci. Total Environ.*, 888, 164 181, <https://doi.org/10.1016/j.scitotenv.2023.164181>, 2023.



- 645 Yang, P., Wei, H., Huang, H.-L., Baum, B. A., Hu, Y. X., Kattawar, G. W., Mishchenko, M. I., and Fu, Q.: Scattering and absorption property database for nonspherical ice particles in the near- through far-infrared spectral region, *Appl. Opt.*, 44, 5512–5523, <https://doi.org/10.1364/AO.44.005512>, 2005.
- Yang, P., Bi, L., Baum, B. A., Liou, K.-N., Kattawar, G. W., Mishchenko, M. I., and Cole, B.: Spectrally Consistent Scattering, Absorption, and Polarization Properties of Atmospheric Ice Crystals at Wavelengths from 0.2 to 100 μm , *J. Atmos. Sci.*, 70, 330 – 347, 650 <https://doi.org/10.1175/JAS-D-12-039.1>, 2013.